

POLITECNICO DI TORINO  
GRENOBLE INP - PHELMA  
ÉCOLE POLYTECHNIQUE FÉDÉRALE DE  
LAUSANNE

Master's Degree in Nanotechnologies for ICTs



**Politecnico  
di Torino**

Master's Degree Thesis

**Development of graphene-based devices for  
vibrations detection**

Supervisors

Prof. Guillermo VILLANUEVA

Prof. Carlo RICCIARDI

Candidate

**Vincenzo MESSINA**

September 2021



# Summary

The aim of this Master's thesis is to provide two possible applications of graphene-based suspended membranes as Nano Electromechanical Systems (NEMS) able to detect vibrations in a sample. The entire project has been carried out within the Advanced NEMS Laboratory at EPFL (Lausanne, Switzerland) under the supervision of Professor Guillermo Villanueva and in part in collaboration with a startup of the EPFL Innovation Park, Miraex.

The research developed during the thesis is described in detail in the six chapters that form this document, which are followed by an appendix containing some Matlab and Python codes used to simplify and speed up data acquisition and the related post-processing part. In the first chapter the trend that M/NEMS market and research have been following in the last decades is described with particular focus on those graphene-based. This is done to contextualize the proposed devices, showing the state of the art and clarifying the purpose of the project. The second chapter presents in detail the structure of the devices used, their peculiarities and how they are manufactured to obtain circular suspended membranes with a very large aspect ratio. Since there are several devices available from previous fabrication, before proceeding with the study of their possible applications, the third chapter deals with the selection process to which all membranes are subjected. More in details, their surface topography is carefully inspected with the help of an optical microscope and a Digital Holographic Microscope. Then, only the membranes with the best surface conditions are exploited in the subsequent analysis. Afterwards, the fourth and fifth chapters are the main ones in which most of the work is concentrated. There, two devices based on graphene membranes are proposed: the first case regards a vibrometer, while the second one a pressure sensor to be integrated into an optical microphone. Considering the former, an analysis is made with the aim of researching the origin of the phenomenon which is at the basis of its working principle, that is the shift of membrane resonance frequency due to an applied acceleration. The resonance frequency of the membranes is studied and also how the latter is affected by external stimuli. In this analysis a Laser Doppler Vibrometer and a DHM in dynamic mode are used for the characterization of the devices. The same measurements are developed on devices with a different

structure or a different material and the results are compared with those obtained for graphene membranes to inspect possible dependencies. While, for what concerns the pressure sensor, firstly, it is studied how to optimize its performance and then, the best layout to integrate it with the optical fiber and realize the microphone is analyzed. In addition, a first attempt at characterizing the device is tested using a loudspeaker and a reference microphone and analysing the frequency response of the microphone. What characterizes both devices is the fact that they are based on optical sensing principles and do not include electronic components. For this reason they are intended to be used in harsh environments with high temperatures or where electronic components do not work properly, as for space or military applications. Finally, in the sixth chapter the conclusions of the research performed are outlined.

# Acknowledgements

I would like to express my sincere gratitude to Professor Guillermo Villanueva for his constant guidance and his availability during every single step of the project. His teachings on how to carry out the research have always been invaluable. I would also like to thank the Miraex group, who followed me during a part of the project allowing me to use their equipment, their collaboration was fundamental. Many thanks also to the various research laboratories that helped me during the project, such as the Division of Micro and Nanosystem at KTH, Sweden, which provided useful material for research, but also the EPFL signal processing laboratory (LTS2) which allowed me to use their anechoic chamber providing me all the necessary instrumentation for the measurements to be performed suggesting me how to improve them. My genuine thanks goes also to the entire ANEMS group, they have always been very helpful and friendly, sharing with me their experiences and guiding me in the laboratory, especially, to Daniel for his help in mounting all the setups for the various measurements and for his tips on how to improve them. Last but not least, a special thanks goes to my family, my parents and my brother who supported and encouraged me throughout this experience, despite the distance they never made me feel alone. Finally, I am extremely grateful to all my friends, near and far, new and of a life, who allowed me to take pleasant and cheerful breaks during this period characterized by constant work and restrictions due to COVID-19 and with whom I have spent special moments and experiences that I will never forget.

*Per aspera ad astra...*



# Table of Contents

<b>List of Tables</b>	VIII
<b>List of Figures</b>	IX
<b>Acronyms</b>	XIII
<b>1 Introduction</b>	1
1.1 Evolution of MEMS and NEMS . . . . .	1
1.2 Graphene . . . . .	3
1.3 NEMS with graphene . . . . .	5
1.4 Purpose of the project . . . . .	7
<b>2 Device</b>	9
2.1 Design . . . . .	9
2.2 Process flow . . . . .	10
<b>3 Selection process</b>	13
3.1 Optical microscope . . . . .	13
3.2 Digital holographic microscope (DHM) . . . . .	14
3.2.1 Working principle and set-up . . . . .	15
3.2.2 Phase adjustments . . . . .	16
3.2.3 Surface topography . . . . .	17
3.3 Improvement of membrane surface through thermal annealing . . . . .	22
3.4 Summary of selected membranes . . . . .	25
<b>4 Accelerometer based on graphene membranes</b>	26
4.1 Theoretical background . . . . .	28
4.1.1 Model and detection chain . . . . .	28
4.1.2 Resonant frequencies . . . . .	29
4.1.3 Responsivity . . . . .	30
4.1.4 Built-in stress . . . . .	31

4.2	Measurements set-up . . . . .	32
4.2.1	Laser Doppler Vibrometer working principle . . . . .	34
4.2.2	Measurements under vacuum . . . . .	35
4.3	Measurements for resonant frequency detection . . . . .	36
4.3.1	Thermomechanical noise study . . . . .	36
4.3.2	Frequency sweep response . . . . .	37
4.3.3	Membranes displacement through DHM . . . . .	38
4.3.4	Resonant frequency and related built-in stress . . . . .	40
4.4	Acceleration measurement . . . . .	42
4.4.1	Acceleration due to a change in voltage . . . . .	44
4.4.2	Acceleration due to a change in frequency . . . . .	46
4.4.3	Responsivity with respect to displacement . . . . .	48
4.5	Measurements reproduced on different devices . . . . .	49
4.5.1	Comparison with 30 $\mu\text{m}$ membrane . . . . .	49
4.5.2	Comparison with SiN membranes . . . . .	51
4.6	Discussion . . . . .	53
4.6.1	Detection of vibrations . . . . .	53
4.6.2	Possibility to remove the mass . . . . .	53
4.6.3	Dependence on dimensions and material . . . . .	54
4.6.4	Possible future improvements of the measurements . . . . .	55
<b>5</b>	<b>Pressure sensor based on graphene membranes</b>	<b>57</b>
5.1	Working principle . . . . .	58
5.1.1	Responsivity . . . . .	58
5.1.2	Responsivity optimization . . . . .	59
5.2	Fabrication and packaging . . . . .	62
5.3	Characterization . . . . .	64
5.3.1	Measure of graphene membrane reflectivity . . . . .	65
5.3.2	Frequency response analysis . . . . .	65
5.4	Discussion . . . . .	68
<b>6</b>	<b>Conclusions</b>	<b>71</b>
<b>A</b>	<b>Codes</b>	<b>74</b>
A.1	Sliding mean . . . . .	74
A.2	Acceleration due to a change in voltage . . . . .	76
A.3	Microphone frequency response . . . . .	79
	<b>Bibliography</b>	<b>83</b>

# List of Tables

3.1	Roughness computed for different window apertures. . . . .	21
3.2	Diameter and roughness of some selected membranes. . . . .	25
4.1	The four columns contain diameters, resonance frequencies, built-in stress and pressure conditions of the various membranes analysed. In particular the last three lines contain the values of the membranes measured under vacuum. . . . .	41
4.2	Data of a $100\mu m$ membrane with a resonance frequency of 386 kHz. Voltage sweep and the corresponding acceleration are obtained from calibration step. Resonant frequency shift is the result of average of 5 independent measurements from which the standard error can also be derived. Responsivity of the device and its standard error are located at the bottom right of the last two rows and are obtained through the equations 4.21 and 4.22. . . . .	46
4.3	Data of a $100\mu m$ membrane with a resonance frequency of 386 kHz. Frequency sweep and the corresponding acceleration are obtained from calibration step. Resonant frequency shift is the result of average of 5 independent measurements from which the standard error can also be derived. Responsivity of the device and its standard error are located at the bottom right of the last two rows and are obtained through the equations 4.21 and 4.22. . . . .	48
4.4	Data of $30\mu m$ diameter graphene membrane. . . . .	51
4.5	Data of silicon nitride membrane. . . . .	52
4.6	Data of graphene membranes without mass. . . . .	55
5.1	Graphene and reference microphone frequency response and ground noise. . . . .	68

# List of Figures

1.1	MEMS sensors & actuators: the 5 senses and many more [1] . . . . .	1
1.2	Miniaturization and diversification trends to obtain systems with improved performances. . . . .	3
1.3	Graphene structure with a highlight on carbon bonds [6]. . . . .	3
1.4	Carbon allotropes derived from graphene [9]. . . . .	4
1.5	Device graphene-based with suspended mass [17]. . . . .	5
1.6	Microphone graphene-based with a capacitive readout [18]. . . . .	6
2.1	Si chip design with a graphene sheet transferred on top (grey rectangle).	10
2.2	Profile of a through-hole chip with suspended monolayer graphene membrane. . . . .	10
2.3	Main steps for transferring graphene from a Cu foil onto the Si chip.	11
3.1	Membranes with different surface conditions under optical microscope.	14
3.2	DHM architecture [31] . . . . .	15
3.3	Effects of the phase adjustments on the hologram . . . . .	16
3.4	Membranes surface under DHM from an intensity, phase and profile point of view. . . . .	17
3.5	Waviness and roughness contributions to surface profile [35]. . . . .	18
3.6	Extraction of roughness from surface profile performed by the Matlab script in Appendix A.1. . . . .	18
3.7	Repeatability Average = 7.45 nm, Standard deviation = 0.38 nm . . . . .	21
3.8	Surface membranes compromised by defects and contaminants. . . . .	22
3.9	Experimental setup for thermal annealing. . . . .	23
3.10	Temperature and pressure control during thermal annealing. . . . .	24
3.11	Thermal annealing steps. . . . .	25
4.1	Results on the dependence of device responsivity due to displacement with respect to membrane built-in stress [36]. . . . .	27
4.2	Model of resonant accelerometer. . . . .	28

4.3	Eigenmodes and their respective $\alpha_{n,j}$ values for a circular membrane [38]. . . . .	30
4.4	Complete experimental setup [16]. . . . .	33
4.5	LDV architecture [39]. . . . .	34
4.6	Thermomechanical noise (a) and parameter setting (b). . . . .	37
4.7	Response of the device due to a frequency sweep around its resonance peak. The legend reports the different driving voltages applied to the piezoshaker to stimulate the membrane. . . . .	38
4.8	2-D profile of the membrane vibrating at its resonant frequency plotted for different time frames. . . . .	39
4.9	Comparison between the displacement of the same membrane at atmospheric pressure and under vacuum. . . . .	40
4.10	Frame of the 3-D reproduction in real time of membrane deflection. . . . .	40
4.11	FFT of frequency data recorded for 10 seconds. . . . .	42
4.12	Calibration of the setup. Measure of provided acceleration due to a sweep in driving voltage and a sweep in frequency. (a) Voltage sweep between 100mV and 500mV with frequency fixed at 160Hz. (b) Frequency sweep between 160Hz and 1000Hz with voltage fixed at 0.5V. . . . .	43
4.13	Shift of the resonant frequency vs Acceleration due to a change in voltage. . . . .	44
4.14	Responsivity with respect to acceleration due to a change in voltage. . . . .	45
4.15	Shift of the resonant frequency vs Acceleration due to a change in frequency. . . . .	47
4.16	Responsivity with respect to acceleration due to a change in voltage. . . . .	47
4.17	Displacement responsivity behavior. Voltage sweep between 100mV and 500mV at a constant frequency equal to 160Hz. Frequency sweep between 160Hz and 1000Hz at a constant driving voltage equal to 500mV. . . . .	49
4.18	Study on the $30\mu m$ diameter membrane with a resonance peak at 1.51 MHz. a) Thermomechanical noise is plotted in V, but the Power spectral density can be easily derived. b) Sweep in frequency is performed and a peak at the same frequency of the one in TMN is detected. . . . .	50
4.19	Shift of the resonant frequency vs Acceleration due to a change in voltage for the $30\mu m$ membrane and responsivity for each acceleration. . . . .	50
4.20	SiN membrane resonance frequency shift and responsivity due to acceleration (voltage sweep between 100mV and 500mV, frequency fixed to 160Hz). . . . .	52

4.21	SiN membrane resonance frequency shift and responsivity due to acceleration (frequency sweep between 160Hz and 1000Hz, voltage fixed to 0.5V). . . . .	52
4.22	Relative displacement responsivity vs membrane built-in stress. The mass-free membrane data are reported in blue (No mass) and are identified through their diameter in micrometers, while the membranes with the mass attached are in yellow (Mass) and the their label indicates the length of one side of the mass in micrometers. . .	54
4.23	Zoom in of relative displacement responsivity vs membrane built-in stress for membranes without mass with a focus on standard errors.	56
5.1	Microphone diaphragm responsivity vs Frequency with an highlight on geometrical dependencies. . . . .	60
5.2	Microphone diaphragm responsivity vs Device bandwidth. . . . .	61
5.3	Microphone layout. The optical fiber is installed on the backside of the graphene membrane and is fixed and supported by a silicon cap and a plastic ferrule. . . . .	62
5.4	Optical fiber glued to silicon cap in correspondence of the graphene membrane on the backside of the silicon chip. . . . .	63
5.5	Setup for the installation of the optical fiber. . . . .	64
5.6	Setup for testing reflectivity of the graphene microphone. . . . .	65
5.7	Setup to study the frequency response of the graphene microphone.	66
5.8	Setup mounted inside the anechoic chamber. . . . .	67



# Acronyms

**APS**

Ammonium persulfate

**CEO**

Chief executive officer

**CLA**

Center-line average

**CVD**

Chemical vapor deposition

**dB**

Decibels

**DHM**

Digital holographic microscope

**DUT**

Device under test

**FEM**

Finite element modeling

**FFT**

Fast Fourier Transform

**IC**

Integrated circuit

**IFM**

Inverted floating method

**IoT**

Internet of Things

**LDV**

Laser Doppler Vibrometer

**MEMS**

Micro electromechanical system

**NEMS**

Nano electromechanical system

**PMMA**

Poly Methyl Methacrylate

**ppm**

part per million

**PSD**

Power Spectral Density

**PZE**

Piezoelectric

**RMS**

Root mean square

**RT**

Room temperature

**Si**

Silicon

**SiN**

Silicon nitride

**SPL**

Sound pressure level



# Chapter 1

## Introduction

### 1.1 Evolution of MEMS and NEMS

The technological development that has distinguished our society for several years seems unstoppable. Nowadays a huge amount of devices is produced daily, devices able to meet any request or need, making our life much better. To describe with a single word the thousands of devices that surround us can be used the term MEMS, that stands for micro electromechanical system. It encloses all the huge variety of sensors, actuators, accelerometers and other miniature systems that are at the base of any smart object of our everyday life. They are able to reproduce the five human senses, improve them and go even further. Some significant examples are listed in Figure 1.1.

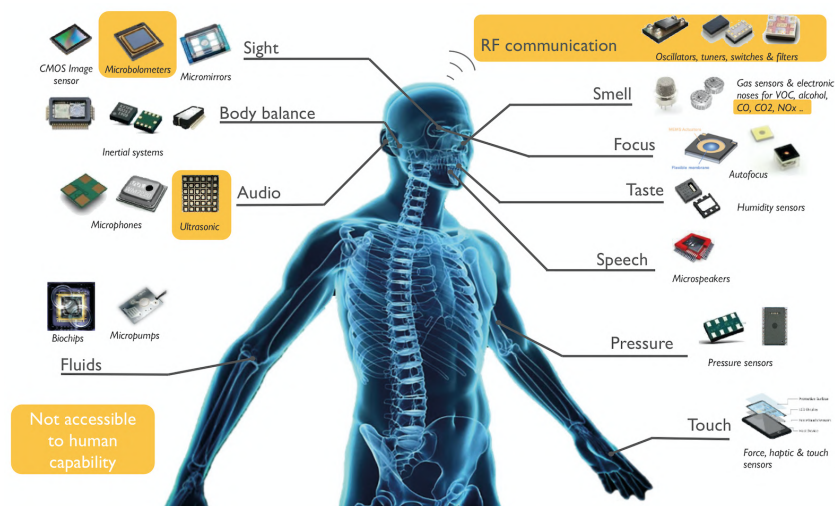
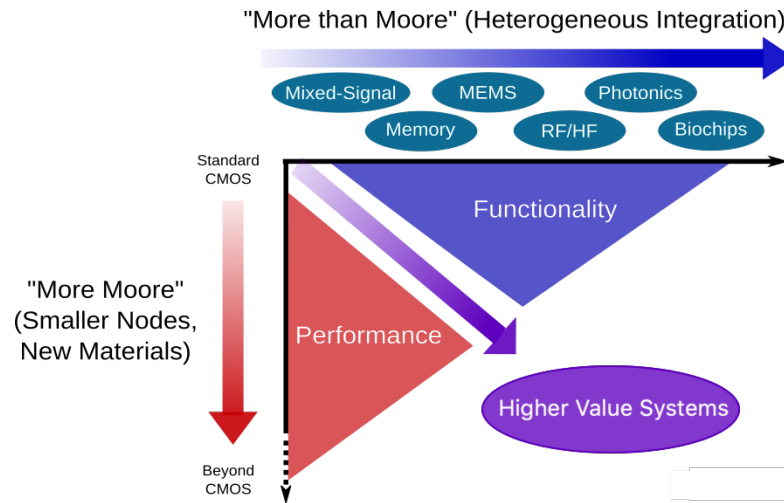


Figure 1.1: MEMS sensors & actuators: the 5 senses and many more [1]

MEMS devices range in complexity from simple structures with no moving parts to highly complicated electromechanical systems with several moving parts, most of the time integrated with microelectronics as a part of a bigger system for various applications, such as biomedical, automotive, consumer electronics, etc. MEMS technology evolved from the Integrated Circuit (IC) industry and become object of attention for research as soon as micromachining techniques for the semiconductor industry have been developed and refined [2]. Between 1960s and 1980s microfabrication and miniaturization started to grow following the trend described by the Moore's law. This law was postulated by Gordon Moore, CEO of Intel, in 1965 based on very few data, but it perfectly describes what is the evolution of the size of the devices, in particular the cell unit of an integrated circuit, the transistor, that is its continuous reduction so much to allow the realization of chips with a number of transistors that doubles every two years approximately. He is one of the two scientists who predicted the future trend of technology towards smaller and smaller sizes. The second one is Richard Feynman with his famous talk "There's Plenty of Room at the Bottom" in 1959 where he showed all his interest in fabricating and manipulating devices down to a nanometric scale and all the benefits that could be derived from them, even anticipating what today are the NEMS, nano electromechanical systems [3]. During 1990s, thanks to significant improvements in micromachining, the field of MEMS is subjected to an acceleration and it has been possible to realize devices with extremely small dimensions and with increasing potential and enhanced performance, compared to the macroscale ones. The continuous miniaturization leads to the realization of the first NEMS, a device that has at least one submicron dimension, and, thanks to it, to the discovery of new physical properties that significantly influence the functioning of these devices. Recently the predicted curve is getting closer to saturation, considering that the structure of many material in terms of mechanical stability and stiffness is compromised reaching the physical limit of one atom. For this reason, research is moving towards new materials and new technologies that can further improve the performance of previous devices, while integrating more functions into the same device. This new trend is defined as "More than Moore" and, instead of describing the miniaturization of the devices, treats their diversification [4]. This diversification leads to the increasingly massive development of new devices that can combine small dimensions with multiple functions obtaining new devices with advanced features. So, despite a general stagnation of the semiconductor industry, MEMS remains a shining star that will lead the future market [1]. M/NEMS devices are evolving towards greater integration not only with microelectronics, but also with emerging technologies capable of manipulating matter at the atomic or molecular level to achieve something never seen before at nanometric scale, reaching a complex integration level called "heterogeneous integration" [5]. All these new trends can be traced through the graph in Figure 1.2, where it can be

noticed towards what progress is moving to get better and better devices.



**Figure 1.2:** Miniaturization and diversification trends to obtain systems with improved performances.

## 1.2 Graphene

Among the revolutionary devices that have been developed in the last years, there is a particular type that exploits the unique properties of carbon-based materials, in particular the ones of graphene, reaching characteristics unattainable with other materials and that can be used for the most advanced NEMS applications. Graphene is an allotropic form of carbon that consists of a single layer of carbon atoms arranged in a hexagonal honeycomb lattice forming  $sp^2$  hybridized orbitals as shown in Figure 1.3.

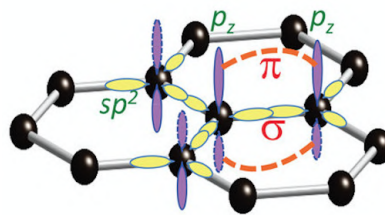


**Figure 1.3:** Graphene structure with a highlight on carbon bonds [6].

The strong covalent bond that binds each carbon atom with the three nearest gives to the single sheet of graphene exceptional tensile strength of 130 GPa and stiffness (Young's modulus) close to 1 TPa [7]. Graphene has also remarkable

thermal properties, with a RT thermal conductivity of up to  $5.30 \cdot 10^3 W/mK$  that demonstrates graphene as a superior thermal management material [8]. Another intriguing feature is its 2-D structure where every atom is in direct contact with the surrounding environment, in this way any external variation could affect directly its electrical or mechanical properties making graphene a perfect candidate for sensing applications. Moreover, being a two-dimensional material, it can be particularly useful to investigate 2-D physics and chemistry, but also to build other carbon allotropes with dimensions reduced to a few nanometers along more directions, like nanotubes (1-D) and fullerenes (0-D), paving the way for a myriad of new applications, such transistors, sensors, resonators, supercapacitors, ecc. [5]. The different kinds of allotropic carbon forms that can be derived from graphene are illustrated in Figure 1.4.

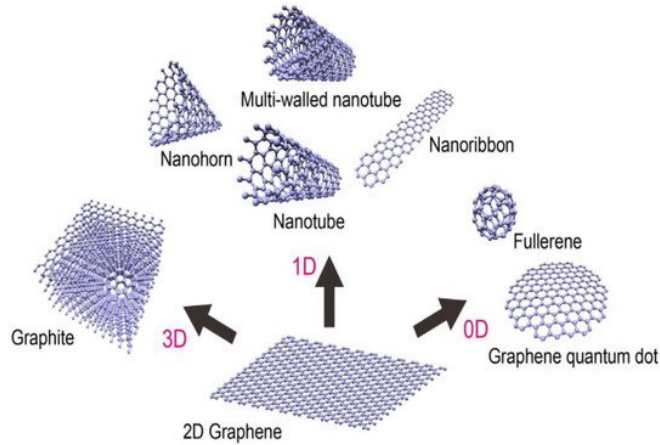


**Figure 1.4:** Carbon allotropes derived from graphene [9].

In the devices developed up to now graphene is also employed composed by two layers or few layers, obtaining almost the same interesting characteristics. The first approach to obtain graphene sheets was mechanical exfoliation from graphite, that basically consists of several layers of graphene placed one on top of the other kept together by van der Waals forces. Thus, by applying exactly the force that binds the first to the second layer, it was possible to remove only one layer without damaging the others. This procedure can be slow and with a low throughput, so different types of alternatives have been studied. The most convenient synthesis method results the one based on CVD because it allows to obtain large membranes with a good quality ready to use [10].

### 1.3 NEMS with graphene

Graphene, thanks to its unique properties and structure, has always attracted the attention of research, since its discovery in 2004 by the scientists Geim and Novoselov at the University of Manchester [11]. This material plays an important role, it is possible to notice how it perfectly aligns with the trend described in section 1.1: the continuous pursuit of miniaturization and diversification. In fact, graphene is the thinnest material in the world with a monolayer thickness of  $\sim 0.335nm$  and, at the same time, it can be used for a wide range of applications yielding increased device performance. Nowadays a huge variety of graphene-based MEMS/NEMS are object of research, for example, thanks to its ultrathin structure that provide extremely high sensitivity, graphene can be helpful for applications that require high precision such biomedical application, nanorobotics or for monitoring seismic activities. At the same time, proceeding with miniaturization of the device surface permits to operate on a wider frequency range up to megahertz, since the smaller the size and the higher is the resonance frequency of the resonator, making these kind of MEMS ideal for communication applications and IoT devices. Moreover, thanks to its superior mechanical and thermal properties, such as high Young Modulus and the possibility of operating even at high temperature (up to  $2000^{\circ}C$ ), graphene has the qualities to withstand harsh environments and can be exploited perfectly for space and military applications. Among the different usages, from a structural point of view, graphene is very promising in the form of beam or membrane. In particular, in the form of a suspended structure, graphene can be used as a mechanical resonator and can be found as beams clamped at one end (cantilever) [12], at both ends [13] or completely clamped [14]. The interesting feature of those membranes is that they can be frequency tuned with different active or passive methods [15] acting on their mass and stiffness. The subject is still object of research, in this work that phenomenon is exploited for the creation of a resonant accelerometer/vibrometer. A similar attempt was made with an accelerometer composed of a graphene membrane with a suspended mass as shown in Figure 1.5, also in that case the device's resonance frequency shift was studied to detect the applied acceleration [16].

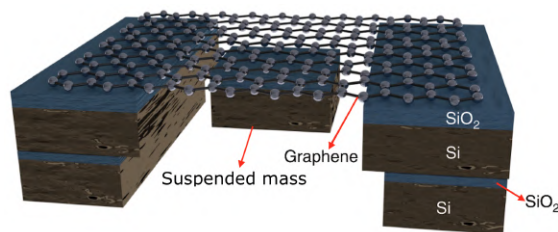


**Figure 1.5:** Device graphene-based with suspended mass [17].

In the present project the same results are aspired, but with a graphene membrane without the mass, this would lead to greater simplicity in the fabrication phase and the possibility of further reducing the size of the device.

Always based on suspended membranes, another application that could take advantage of ultra light weight and extremely reduced size, is a high performance and miniaturized microphone. Different types can be fabricated, which are distinguished according to the material employed or the readout mechanism of membrane displacement, that can be capacitive [18], optical [19], thermal [20], ecc. But the basic building block that is present in each device is a pressure sensor that deflects when stimulated by an acoustic wave, in the case of a receiver, or that generates an acoustic wave when behaves like a transmitter. An example of an existing microphone graphene-based is reported in Figure 1.6, where the pressure sensor is composed by a graphene membrane and two spacers, while the readout mechanism is capacitive, as can be deduced from the presence of two electrodes.

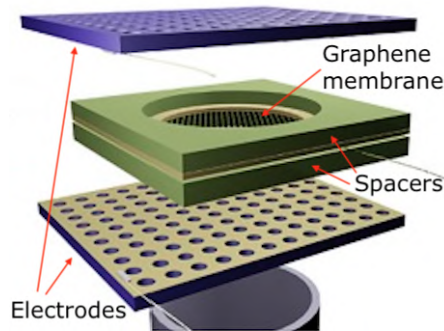


**Figure 1.6:** Microphone graphene-based with a capacitive readout [18].

Some patents have already been published by Apple and Samsung of microphones and speakers based on graphene membranes or on heterogeneous structure with the presence of a graphene membrane [21]. These devices exploit the electromechanical transduction properties of graphene and could be used to replace the current microphones installed in portable devices such as mobile phones, tablets or pc, since it gets more difficult to deliver high-quality audio devices using standard materials as devices become smaller and lighter. Enormous progress has been achieved in NEMS technology that adopts carbon-based materials obtaining enhanced performances unreachable with other microscale devices, but, even today, it is not possible to reproduce them on industrial level, because a fully control of their properties is not achieved yet, especially if they are composed by large surfaces that are easily influenced by the external environments [22]. For this reason new fabrication processes [23] or post-fabrication processes [24][25] are adopted to improve surface condition.

## 1.4 Purpose of the project

The project aims to study surface conditions of suspended graphene membranes with a very high aspect ratio fabricated through a transfer process via PMMA followed by a thermal annealing treatment under vacuum to obtain the most regular and clean membranes possible. This study is essential for a better understanding of their properties and the possible origin of the problems that limit their industrial application. In fact, before inserting graphene membranes into a manufacturing process at industrial level and implementing them into commercial devices, it is necessary to carefully explore every fundamental aspect and characterize their features in detail. Particular attention has to be paid to surface conditions in terms of contamination, defects and surface roughness, especially when the desired membranes have a large area [22]. This work would like to help the development of this research field providing information about the surface of graphene membranes with large diameter up to  $750\ \mu\text{m}$  and thickness of one or two atoms, using monolayer and bilayer graphene sheets. The current problems encountered during fabrication relate to the formation of defects on the surface that alter their mechanical and optical properties affecting performance. These defects can be caused accidentally while transferring graphene, in fact this is a very delicate process and would need to be automated in such a way as to be carried out with very high precision in order to achieve the same results on all membranes. Other issues are caused by the possible presence of residues that contaminate the surface altering electrical and chemical properties of the devices, but also causing adhesion problems. This study is a continuation of a previous work that had the aim of removing contaminant particles through thermal treatments carried out after the manufacturing process obtaining ultra clean membranes with enhanced mechanical properties [26].

In addition, two possible applications of these graphene membranes are proposed: a singular type of mass-free vibrometer and a pressure sensor that can be integrated into a microphone for applications in harsh environments. The purpose of the project is to inspect new potentiality of graphene, that with its extreme properties could lead to development of new and advanced NEMS, improving the existing ones and substituting them on a wide range of applications. As a vibrometer, graphene membranes can be used to sense a displacement in a sample with an extremely high responsivity, combining this with miniaturized dimensions. The proposed device is based on a suspended monolayer graphene membrane that acts as a resonator and changes its resonance frequency according to an applied vibration. This is possible thanks to the high surface-to-volume ratio of the membrane that causes the resonance frequency to depend mainly on in-plane tension, that in turn can be modified by applying a vibration that deforms the membrane. The change in resonance frequency is detected through a LDV, while vibration is provided through a piezoshaker. A study of the resonance frequency of the membranes is also

performed in relation to their diameter by comparing membranes with diameters ranging from  $30\mu m$  to  $750\mu m$ . To prove the consistency of the measurements and to confirm that the shift of the resonance frequency is not a random phenomenon appeared only in those specific devices, a comparison is made with other two devices: a similar one composed also of a graphene membrane, but with a silicon mass above and a membranes in silicon nitride.

For what concerns the pressure sensor, other properties of graphene are taken into account, in particular the mechanical and thermal ones. Thanks to its extremely high Young's modulus and its endurance even at high temperature, the proposed sensor can withstand very large pressures and operate in harsh environments with temperatures up to  $2000^{\circ}C$ . At the same time it maintains a high sensitivity and can work in a wide range of frequency, even higher than  $100kHz$ , thanks to its ultra thin thickness and large diameter ( $D > 300\mu m$ ). All these features make it the ideal device for space or military applications. Moreover, what differentiates it from other microphones based on a graphene membrane is the readout system, that is all optical based on a optical fiber that detects the membrane displacement. This matches the harsh environment conditions and does not need a particularly robust setup, as required in the case of a readout system based on interference, since it is already quite stable over a wide range of operational parameters.

# Chapter 2

## Device

This chapter deals with the description of the structure of the devices used in this project and their manufacturing process. They have been the subject of a previous study carried out in the Advanced NEMS Laboratory at EPFL which aimed to obtain graphene membranes with a very high aspect ratio, a high reproducibility and improved dynamic mechanical properties thanks to a thermal annealing process to which the membranes are subjected immediately after manufacture. This research was successful and published in Nature [26].

In this research the same devices are exploited to study some of their possible applications. In particular, in a first case they are employed to analyze if their resonance frequency can be directly influenced by an external applied acceleration and, if true, how it is affected. Secondly, it is inspected the possibility of using these devices to create pressure sensors able to detect an incident acoustic wave through the deflection of the membrane and, successively, integrating them into an optical microphone.

### 2.1 Design

The devices used in this project have a simple geometry. They are circular membranes of different diameters made by monolayer and bilayer graphene. These membranes are obtained by transferring graphene sheets onto silicon chips with predefined holes as deep as their entire thickness. Graphene adheres to the silicon substrate and remains attached to it by van der Waals bonds forming a diaphragm over the corresponding holes. In this way it is possible to obtain circular suspended membranes with different diameters depending on the hole size. Since the graphene transferred has a smaller area than the silicon chip, not all devices have each diameter available, for this reason they are subsequently classified. The design

in detail of the silicon base chip is shown in Figure 2.1, where, in addition to the arrangement of the holes over the chip, their diameter ranging from  $10\mu m$  to  $1000\mu m$  is also shown. The gray highlighted rectangle on the chip indicates a possible layout of the transferred graphene sheet and was inserted as an example to better get an idea of the device.

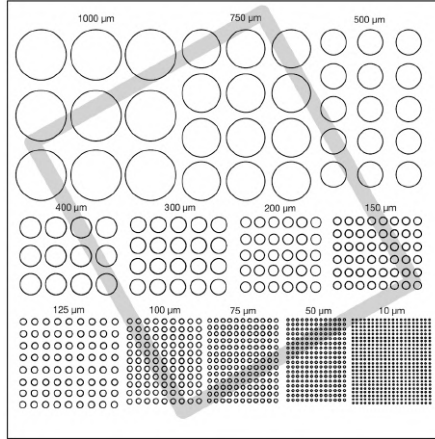


**Figure 2.1:** Si chip design with a graphene sheet transferred on top (grey rectangle).

In addition to the front view of the chip (Figure 2.1), a cross-section view of its profile is also reported to have a full description of the device (Figure 2.2). For the sake of simplicity the profile of a single hole with its suspended membrane is shown.



**Figure 2.2:** Profile of a through-hole chip with suspended monolayer graphene membrane.

A peculiarity of these membranes is their huge aspect ratio, with diameters that can potentially reach  $1mm$  and thickness of less than  $1nm$ .

## 2.2 Process flow

In order to synthesize thin films of graphene different techniques can be exploited, these can be classified in many ways based on the type of carbon source or the preparation technique. There are direct and indirect methods for the transfer, among which it is possible to choose depending on the desired results [27]. The main methods used to synthesize few layers of graphene are three: chemical vapor deposition (CVD), mechanical exfoliation and chemical exfoliation [28].

For the realization of the membranes employed in this project, CVD graphene has been used, it is grown on both side of a copper foil and can be distinguished in monolayer and bilayer. The process consists in transferring the graphene on top of a silicon chip which presents many holes over the entire surface with different diameters ranging from  $10\mu\text{m}$  to  $1000\mu\text{m}$ . The chip is fabricated through a few steps of dry etching of silicon and silicon oxide from both sides until getting the desired holes. While, for the transferring of graphene, a resume of the steps is reported below:

1. Spin coating of PMMA over the CVD graphene grown on Cu foil
2. Etching backside graphene with oxygen plasma
3. Etching Cu foil with Ammonium Persulfate
4. Rinse the graphene with deionized water
5. Transferring on the through-hole chip
6. Evaporate the water between graphene and perforated substrate
7. PMMA removing by IFM exposing it to acetone
8. Optical and SEM measurements
9. Thermal annealing

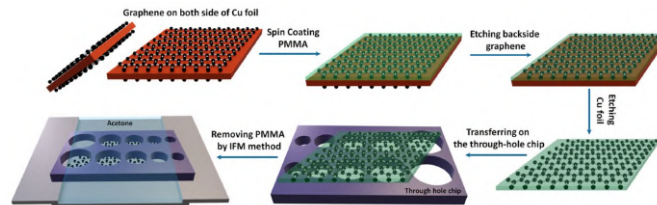


**Figure 2.3:** Main steps for transferring graphene from a Cu foil onto the Si chip.

The first step consists in coating the CVD graphene with a layer of PMMA 150 nm thick. Polymethylmethacrylate (PMMA) can be used to transfer CVD graphene from a metal catalyst, in this case copper, to a substrate, silicon. This method permits to obtain continuous graphene films reducing cracks and defects, in contrast with graphene transfer tape method, which is another transfer method quite used that is easier, but it does not lead to performing results as the PMMA one. Second step expects to remove the backside graphene, since there are two graphene films, one for each side of the Cu foil. Etching is performed through oxygen plasma, a dry

etching method for the removal of organic materials, that is cleaner and safer than other dry etching chemistries. While, regarding the copper foil, it is etched from the PMMA/graphene stack with an ammonium persulfate solution. It takes almost 3 hours, but the duration depends on the concentration of APS in the solution. After removing copper, the left stack is rinsed with de-ionized water for 24 hours. During rinsing it is very important to do not touch the graphene, in order to not introduce defects or breaks, for this reason a pump is used to add and remove water several times from the beaker. After this step, it is possible to perform the wet transfer of graphene onto the Si chip, the latter has a layer of silicon oxide with a thickness of 300nm on top to avoid electrical contacts between graphene and silicon, even if for the application reported below is not a fundamental aspect, since both readout mechanism and working principles are optical based. The PMMA/graphene stack is left onto the through-holes chip for 24 hours at room temperature to let the water evaporate, it is crucial that the environment is dry and extremely clean so as to not introduce contaminants while graphene and the perforated substrate come into contact. To speed up this step, it is possible to perform an annealing of 1 min at 150°C, even if this could lead to some membranes rupture due to water surface tension. Final step consists in removing PMMA by an inverted floating method (IFM), doing so PMMA is exposed to acetone without letting the solution enter into the holes, as shown in Figure 2.3, this lasts almost 5 minutes after which the chip, with the graphene stacked on top, is placed in a vertical position to enhance the cleanliness of graphene surface reducing the presence of possible residues. Finally, to further improve membranes mechanical properties, they are subjected to a thermal annealing of 2 hours at 250°C with a vacuum of  $10^{-4}$  mbar. It is noticed that during this step some membranes break, especially the ones with larger diameters, this could be caused by mismatch of thermal expansion coefficient between graphene and silicon. If a large suspended membrane is desired, another interesting aspect to consider is the average dimension of the graphene grains. Increasing grain size, the possibilities of rupture during fabrication are reduced, as the presence on wrinkles on the surface.

This process is very delicate and requires some experience to achieve good results, especially in the wet transferring of graphene on top of silicon chip. Despite this, it is able to provide membranes with very high aspect ratios and, thanks to the thermal annealing process that follows manufacture, it is possible to get even better results from the point of view of cleanliness and properties of the device. Making these membranes the ideal candidates for this project.

# Chapter 3

## Selection process

Since those membranes were previously fabricated, their surface is not so clean and presents some defects, but although these drawbacks it is possible to still use some of them for the purpose of inspecting the behaviour of graphene membranes subjected to different stimuli. In fact in the following paragraphs it is described the whole process of selection of the membranes and the characterization of these latter, always taking into account the influence of irregularities on the surface of the membranes.

### 3.1 Optical microscope

Every silicon chip is firstly subjected to a quick inspection with an optical microscope. The optical microscope used is the ECLIPSE LV150-N from Nikon, that, thanks to its optical system, is able to combine a high numerical aperture and a long working distance. This is very helpful when high magnification is needed to inspect the sample, since increasing the magnifying power, the working distance is reduced and if not too much attention is paid, you could damage the sample by touching it with an objective lens. The lenses mentioned are the T Plan EPI SLWD (Super-long working distance) with a magnification of 20x or 50x and a working distance of around 22 mm [29]. To further ease the selection process the microscope is equipped with a digital camera (DS-Fi3), that communicate with an imaging software, NIS-Elements, through which it is possible to inspect the membrane surface looking for the presence of contamination or breakage and at the same time, with a tool, to distinguish and characterize the membranes by measuring their diameter. This step allows to make a first selection of the membranes, even if it is not so easy to study single and double layers of graphene due to their very low optical reflectivity, less than 0.2% [30]. But, despite their almost transparency, it is still possible to distinguish the broken one and the presence or not of residues on top of them.

When there is a graphene sheet a contrast between the black background on which the membrane is suspended and its surface is visible, as shown in Figure 3.1. In some cases, it is also possible to observe the size of graphene grains.

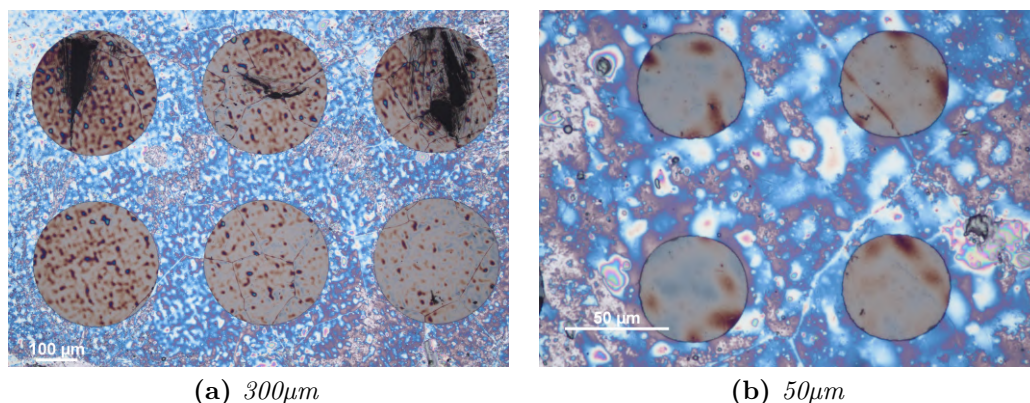


**Figure 3.1:** Membranes with different surface conditions under optical microscope.

The chips with the graphene sheets on top reported in Figure 3.1 have clearly survived the transfer process and the storage period, except the three membranes at the top of Figure 3.1a. Those three are full of defects and breaks, their rupture may be caused at the time of graphene transfer or during the drying step, for this reason they can not be used for the purpose of the project and, obviously, do not pass the first selection step. The others have intact membranes with very few defects and some residue of PMMA, that are represented by the many blue dots scattered over the entire surface of some membranes. Later on, an attempt to remove these contaminants will be exploited to obtain better surface, like the one in Figure 3.1b, that are the best candidates for subsequent measures. Another aspect to note is the size of the membranes and their endurance, in fact, the membranes with the smallest diameter are those that have survived more easily and with a better surface, while larger membranes have, on average, more defects and breakages. The difference is also due to the grains size used during manufacture, which, in this case, are very large and entirely cover some of the smaller holes. Furthermore, it has been demonstrated that the yield of membranes depends also on the grain size, obtaining higher yield for bigger grain size [26].

## 3.2 Digital holographic microscope (DHM)

To further inspect the quality of the membranes, a second step of selection is performed, this time using a more precise and innovative microscope, the digital holographic microscope, in particular the DHM<sup>®</sup> R2100 from Lynceetec.

### 3.2.1 Working principle and set-up

Digital holographic microscopy is an innovative imaging technique that permits to observe a sample through its 3D reproduction. What differs from all the other microscopes is that, not only the intensity of the laser is recorded, but also the phase and this permits to reconstruct the hologram of the sample through a reconstruction algorithm. The working principle of the device is based on interferometry, in particular on the interference between a reference beam and the one reflected by the sample. To obtain an interference path a coherent source has to be used, the available configuration permits to choose between two laser sources. The set-up for these measurements is based on a Mach-Zehnder interferometer with an off-axis geometry as reported in Figure 3.2. There are two types of DHM architectures, one based on transmission and one on reflection depending on the type of sample to be analyzed. The reflection configuration is used in this project.

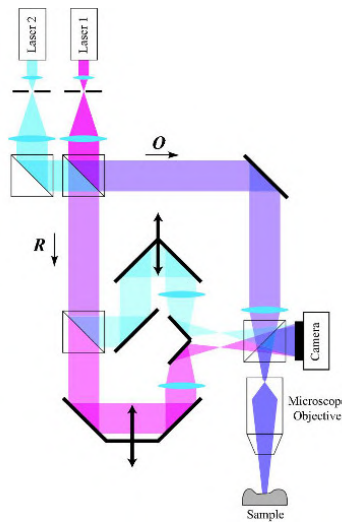


Figure 3.2: DHM architecture [31]

The interference between the two sources generates a synthetic wavelength that enhances microscope performance allowing sub-nanometer vertical resolution, but each wavelength can also be used individually. The peculiar architecture, which combines three beam splitters, some beam expanders and several mirrors, guides the laser beams through two optical paths, one is traversed by the reference wave (R) and the other one by the object wave (O), which is reflected by the sample and then interferes with the first one giving rise to the hologram, whose intensity is routed directly towards a CCD camera. There, thanks to the powerful performances of modern computers and digital cameras, the hologram intensity, containing all the information about intensity and phase of the two waves, is acquired and analyzed. Information about the phase reveal and are used to reconstruct the surface of the

sample with an extremely high vertical resolution in the order of few nanometers, while the intensity provides an image equal to the one of optical microscopes. But what makes these measurements possible is the off-axis configuration which permits to reproduce the hologram of a non transparent sample simplifying the separation of the real and the virtual image produced by the interference of the two waves [32]. This particular configuration leads to a high acquisition rate, few microseconds, that, as a consequence, allows to exploit interesting features such real time measurements with control on the entire sample surface, but also insensitivity to vibrations. All this is what makes the DHM unique and ideal for achieving different goals, in fact this device is able to provide a huge amount of information of in-plane and out-of-plane parameters from both a static and a dynamic point of view.

### 3.2.2 Phase adjustments

After the first selection step, each membrane is analyzed through the digital holographic microscope. As first parameter, the roughness of each membrane is computed, these information are reconstructed from the recorded phase, but some crucial steps are necessary to obtain clear and reliable profile images. Indeed, there are some optical aberration to be compensated, they are introduced by the microscope set up and, in particular, by the microscope objective, that deforms the wavefront causing blurring and flickering images. A digital phase mask is exploited to perform the aberrations compensation, it is calculated automatically by a software that bases phase reconstruction on values extracted from line profiles, indicated by the user, along which the surface is considered flat and is taken as a reference. So, as first step to obtain good quality images, two perpendicular lines, one vertical and the other horizontal, are traced on a flat surface close to the sample (3.3b).

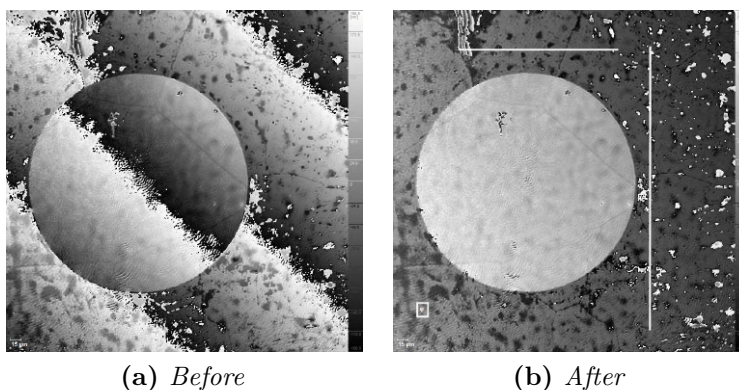


**Figure 3.3:** Effects of the phase adjustments on the hologram

As it is possible to observe in Figure 3.3, after some adjustment the reconstructed phase is much clearer. At this point it is possible to proceed with a study of the surface of the membrane.

### 3.2.3 Surface topography

The analysis of membranes surface is performed through the inspection of their profile. To obtain the required data a tool of the DHM is exploited, it permits to draw straight lines along the image of the reproduced phase and to obtain the profile of the sample section along that direction.

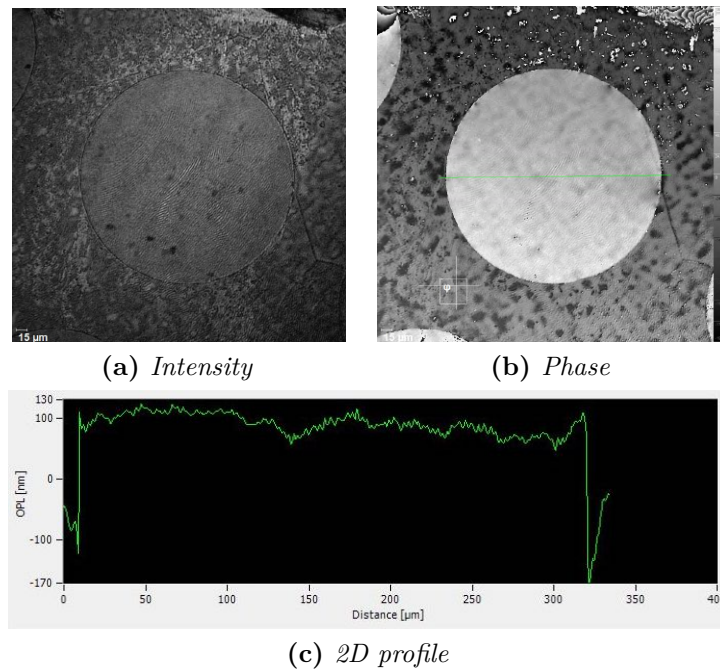


**Figure 3.4:** Membranes surface under DHM from an intensity, phase and profile point of view.

The surface profile is a 2D digital reproduction of the surface morphology, an example of the data obtained is reported in Figure 3.4, where there are the reconstructed intensity and phase of the sample in the upper images, with a green line in the phase one along which the membrane profile is calculated. To study the topology of the surface several acquisition are taken with regular intervals  $\Delta x$  along the traced line, obtaining the image at the bottom of Figure 3.4. A zoom on the surface is performed, taking into account only the data regarding the high step, that represents the membrane under study and that contains all the information about its nano-roughness. A surface profile is usually composed by the superposition of features that act on different length scales, for example it is possible to distinguish between roughness, produced by irregularities of short wavelengths, and waviness,

that, on the contrary, is produced by longer wavelengths [33][34]. An explanatory image is shown in Figure 3.5.

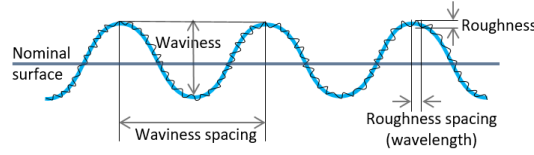


**Figure 3.5:** Waviness and roughness contributions to surface profile [35].

So, to extract only the information regarding the membrane roughness, a sort of "filter" has to be applied to the collected data. In particular, it has the task of separating the contribution of the waviness and removing it from the profile of the previously reconstructed surface. The work of this filter is implemented in a Matlab script (Appendix A.1), where, after saving the data in the appropriate structures to facilitate their management, a moving average is performed throughout the profile. After scanning the entire profile, the average is subtracted from the whole, thus obtaining the roughness isolated from the rest. A useful feature of the script is the possibility of modulating the cutoff length, that determines the range dimension in which values are averaged, in this way you can select the smoothness of the waviness to subtract. In order not to lose any useful information about the roughness of the surface, a smooth waviness is calculated, with a cutoff length not too small so as to not go to subtract from the profile most of the irregularities. An example of the results obtained through the Matlab script is shown in Figure 3.6, where the profile obtained initially by DHM is plotted in red, in black the waviness calculated by the moving average and in blue the final roughness, which will be analyzed.

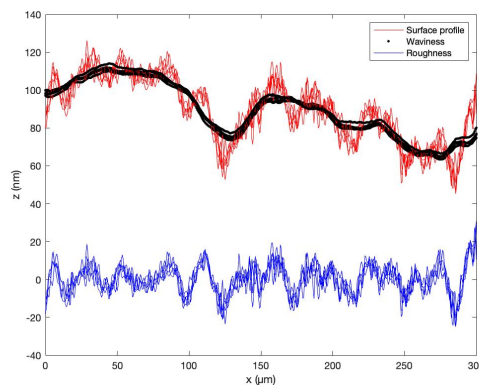


**Figure 3.6:** Extraction of roughness from surface profile performed by the Matlab script in Appendix A.1.

As can be seen, that misleading trend has been removed from the curve, which would have compromised the roughness data. Moreover, in Figure 3.6 it is possible to observe also several overlapping curves of the same colour. This is due to the fact that each measurement has been repeated five times in such a way that, after calculating the parameters characterizing the roughness, their mean and standard deviation can also be derived, so as to perform a more correct and reliable study, since the different acquisitions are subjected to some noise.

According to the International Standardization Organization (ISO) and the American National Standards Institute (ANSI), four main parameters are usually used to completely describe the roughness of a 2D surface profile [33]:

- Center-line average (CLA), the arithmetic mean deviation from the average height, that is denoted by the symbol  $R_a$

$$R_a = \frac{1}{N} \cdot \sum_{i=1}^N |z_i - \bar{z}| \quad (3.1)$$

- Root mean square (RMS), the standard deviation of the surface heights distribution, denoted by the symbol  $R_q$

$$R_q = \sqrt{\frac{1}{N} \cdot \sum_{i=1}^N (z_i - \bar{z})^2} \quad (3.2)$$

- Sweness, it is related to the asymmetry of the heights distribution curve and is represented by the symbol  $R_{sk}$

$$R_{sk} = \frac{\frac{1}{N} \cdot \sum_{i=1}^N (z_i - \bar{z})^3}{R_q^3} \quad (3.3)$$

- Kurtosis, it is related to the sharpness of the heights distribution curve and is represented by the symbol  $R_{ku}$

$$R_{ku} = \frac{\frac{1}{N} \cdot \sum_{i=1}^N (z_i - \bar{z})^4}{R_q^4} \quad (3.4)$$

Previous formulas are reported in their digitized expression, where N is the number of measurements performed along the profile length, while  $\bar{z}$  is the roughness average height, which is taken as reference by each parameter and is equal to

$$\bar{z} = \frac{1}{N} \cdot \sum_{i=1}^N z_i.$$

Since these parameters are statistical descriptors of the heights, they are subjected to random statistical variations, so, as previously mentioned, their mean value and their standard deviation are computed taking the same measurements several times.

For the analysis of the graphene membranes only the second parameters,  $R_q$ , is considered, since the skewness,  $R_{sk}$ , and the kurtosis,  $R_{ku}$ , are rarely used, while the  $R_a$  is unable to distinguish between profiles with different frequency or shape, resulting in profiles with the same  $R_a$  despite one has high and narrow features and the other low and wider ones. In fact, both will give to  $R_a$  the same contribution having the same area, despite the different heights. To compensate this issue, the RMS parameter is exploited, since it is more sensitive to large variations from the average height ( $\bar{z}$ ) [34].

The value of  $R_q$  is computed for many membranes, it is possible to classify them according the number of graphene layers: monolayer or bilayer, but also their diameter. From a first inspection, as regards graphene layers, monolayer and bilayer membranes, under the same conditions, that means considering two membranes with a continuous surface without interruption and without contamination, have the same roughness and it is almost impossible to distinguish them. While a minimal distinction can be made from the point of view of diameter, in fact, as mentioned previously in section 3.1, membranes with smaller diameters, on average, have the surface in better conditions. Despite this, membranes have been found in excellent condition even with larger diameters, up to  $750\mu m$ , naturally in fewer numbers than those with smaller diameters, that go down to  $75\mu m$ . All this demonstrates that graphene is a very resistant material, since, after some months, it is still intact and suspended on silicon chips, despite not being treated too carefully, leaving it at room temperature and atmospheric pressure.

To be more accurate and to give numerical values to the observations, the parameter  $R_q$  is calculated. According to the aperture of the filtering window, the roughness for the same surface profile varies. This is because a surface is composed by many length scales of roughness superimposed on each other, so changing the dimension of the window alternatively some roughness contributions are hidden or filtered and others are revealed, measuring always a different contributions. For this reason roughness parameters are not unique [33]. Their behavior is shown in Table 3.1, where the root mean square parameter ( $R_q$ ) is computed for different membranes varying the aperture of the filtering window. By enlarging the window less and less waviness or other contributions are filtered and thus the roughness increases. The best value for window dimension, so that the main roughness contributions are not filtered and with them important information about the surface, is around 50 points. Lower values would eliminate the contribution made by the presence of contamination, while higher values would not filter enough the contribution of waviness hiding roughness.

Window aperture	Roughness (nm)		
	75 $\mu$ m	100 $\mu$ m	125 $\mu$ m
10	2.76	4.72	7.40
50	5.21	7.87	17.39
100	7.38	9.88	19.46
250	11.15	11.19	21.78

**Table 3.1:** Roughness computed for different window apertures.

After choosing the optimal window aperture, it is possible to continue with the selection of membranes, going to choose those with the lowest roughness, which implies a better integrity of the surface.

Before continuing with other membranes, the repeatability of the measurements is also computed, then different measurements of the same profile are taken and their mean and standard deviation are calculated.

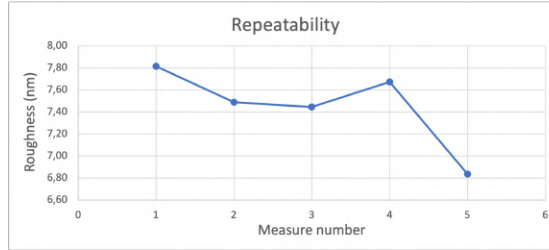


**Figure 3.7:** Repeatability Average = 7.45 nm, Standard deviation = 0.38 nm

From the results shown in Figure 3.7 it can be noted that the standard variation (0.38 nm) is much lower than the average value (7.45 nm), establishing the reliability and the consistency of the measurements and their acquisition technique.

Only few measurements are reported in Table 3.1, but analyzing the results of several measurements, it is noticed that, on average, membranes with smaller diameters have a lower roughness, this can be explained by the fact that having a smaller surface the probability of being contaminated is lower, but also by remembering that these membranes are fabricated using graphene with large grain size, this increases the yield and at the same time reduce the probability of having the edge of a grain crossing a hole, which could cause some rupture or difference in height along the membrane surface.

Studying the different values of  $R_q$  obtained quite good roughness can be noticed for some membranes, ranging around 5 and 10 nm, while for others even higher values are reached, more than 30 nm in worst cases. Two of the worst cases are reported in Figure 3.8. Inspecting their phase and their profile it is possible to observe that they are crossed by a grain edge (Figure 3.8a) or

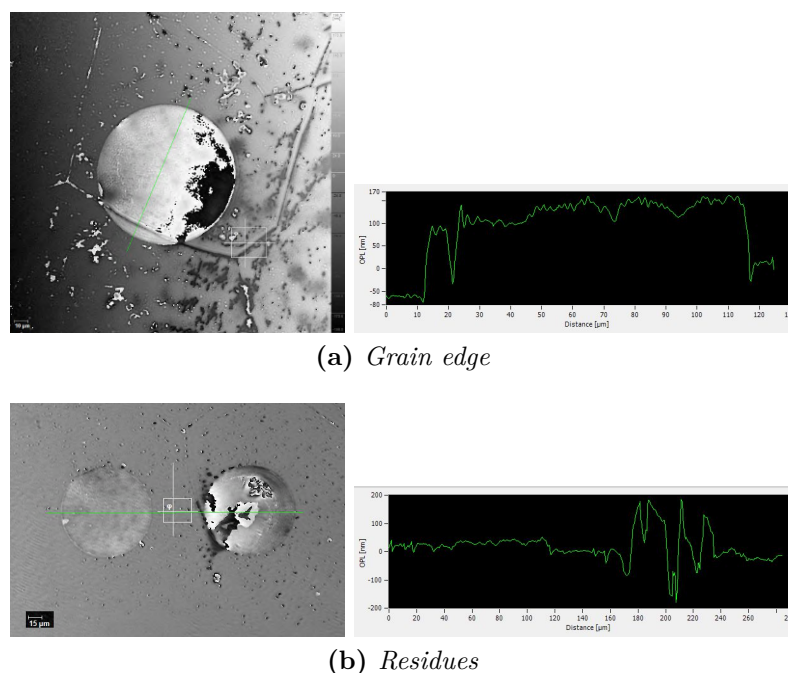


**Figure 3.8:** Surface membranes compromised by defects and contaminants.

contaminated by residues (Figure 3.8b), possibly PMMA or other materials left during fabrication. For the first one almost nothing can be done, instead for the contaminated membranes it is possible to perform a thermal annealing with the purpose of removing the residues if they are organic and at the same time relax the graphene sheet, further reducing the roughness and improving the cleanliness of the surface, trying to obtain better membranes. The thermal annealing process is described in detail in paragraph 3.3.

### 3.3 Improvement of membrane surface through thermal annealing

The thermal annealing process was performed on the membranes with excessive roughness trying to improve their conditions and obtain a cleaner surface. The process consists of subjecting membranes to a period of time at high temperature and under vacuum. Different studies have been led to obtain as much as possible a clean and flat surface free from possible PMMA or organic residues [25]. In fact, transferring the graphene with the PMMA could leave a thin layer of this polymer on top of the graphene altering its properties. Although removing the PMMA residues is not so easy, a thermal annealing could help. Initially to test the

endurance of the membranes it was tried to gradually increase the temperature by  $100^{\circ}\text{C}$  at a time, constantly controlling their surface via DHM. Since the membranes resisted to increasing temperature, this was brought up to  $350^{\circ}\text{C}$ , the maximum attainable with the available instrumentation. At this point the membranes are left at maximum temperature for 2 hours, being monitored in real time via DHM. All this happens only after placing the membranes under vacuum down to a pressure of  $1 \cdot 10^{-3}\text{mbar}$  to facilitate the removal of residues.

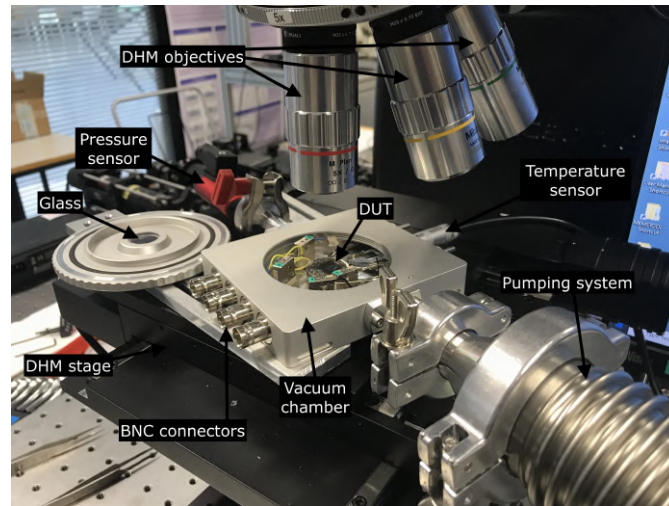


**Figure 3.9:** Experimental setup for thermal annealing.

The entire process is possible thanks to the help of a vacuum chamber, more precisely the HFS350EV-PB4 from LINKAM. Several set-ups have been tested in the laboratory with the instrumentation available to combine different requests: being able to place the vacuum chamber exactly under the objective of DHM, so that the membrane surface can be controlled without having to wait until the end of the process; connect the vacuum chamber to the pumping system in such a way as to reach the desired pressure value in the shortest possible time, then using pipes with a large diameter and through a linear path; secure the vacuum chamber firmly so as to reduce noise due to vibrations produced by the pumping system. The best set up is shown in Figure 3.9, the vacuum chamber is fixed directly to the stage of the DHM so that it is possible to control the position through a joystick and at the same time record the membrane data through a glass in the chamber that allows to see inside. With regard to temperature and pressure control, a software is used which communicates with two sensors located inside the chamber to monitor the two parameters. The stage inside the chamber, on which the chips are placed, is cooled or heated to adjust the temperature reaching the desired one. Through the software it is also possible to set the temperature of the stage by inserting ramps, choosing the desired heating/cooling rate to reach a given temperature and waiting

periods during which temperature is maintained constant, as shown in Figure 3.10.

This process is performed on the membranes with the highest roughness, in general on those which differ most from the average roughness and which have more residues. During the process, data are collected every time the temperature increases by 100 °C till reaching the maximum temperature of 350 °C, once reached it is maintained for 2 hours and the data is collected every thirty minutes.

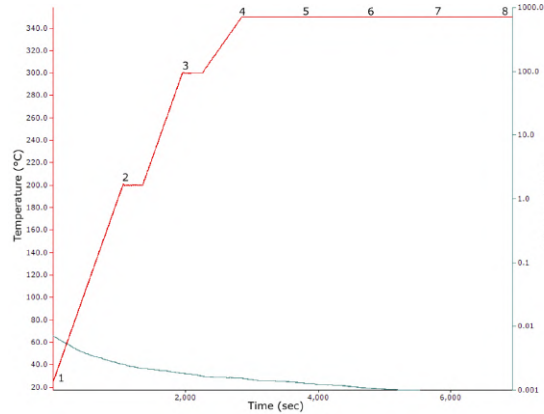


**Figure 3.10:** Temperature and pressure control during thermal annealing.

For the first experiments a low heating rate of 5 °C/min is used to increase the temperature inside the chamber, this because the difference in thermal expansion coefficient between graphene and the silicon surface could led membranes to collapse or could introduce some breaks along the surface. After the first attempts without breaks, it was tried to increase the heating rate to speed up the process, as shown in Figure 3.10, where it is quickly reached a temperature of 200 °C, then 300 °C and more slowly it is increased to 350 °C. In Figure 3.10 is possible to observe also the behavior of pressure with the scale in *mbar* on the right, that decreases during the whole process exponentially reaching values close to  $1 \cdot 10^{-3}$  and below.

Each time 5 acquisitions are made in order to calculate the average roughness trend and the standard deviation and partially reduce the contribution of noise. In fact, a minimum noise is introduced by the vibrations of the vacuum pumping system and by the increase in temperature. The measurements are also very sensitive to minimal movements and even small vibrations can compromise the calibration made initially to compensate the phase, for this reason it is necessary to be very careful during data acquisition. After recording all the necessary information, the data are saved in special structures through a Matlab script (Appendix A.1), a matrix is created and filled with data from the surface of the membrane, the roughness is calculated as described above in paragraph 3.2.3 for each step and the trend is plotted considering the average and the standard deviation each time. Several membranes were subjected to this process, but all showed similar behavior.

An example of the obtained data is reported in the graph in Figure 3.11.

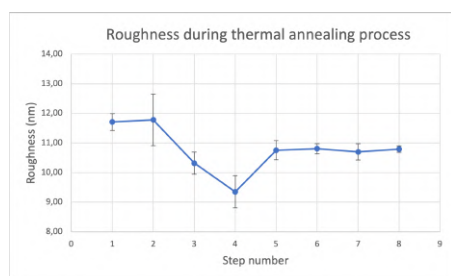


**Figure 3.11:** Thermal annealing steps.

1. Before thermal annealing
2. 200 °C
3. 300 °C
4. 350 °C
5. 350 °C after 30 minutes
6. 350 °C after 1 hour
7. 350 °C after 1 hour and 30 minutes
8. 350 °C after 2 hours

As it is possible to notice membrane roughness does not improve after the thermal annealing process, it remains almost constant with values that are more or less within the margin of error obtained for each measure. The only time that the roughness decreases is as soon as temperature reaches 350 °C, but this data can be considered an outlier caused by external disturbances.

The almost constant trend of membrane roughness throughout the process can be explained by the fact that immediately after their fabrication, the membranes had already been subjected to a very similar thermal annealing process, therefore the surface condition of the membranes had already been improved previously [26] and the roughness cannot be further reduced.

### 3.4 Summary of selected membranes

After inspecting a large number of membranes and studying their surface, only a few were chosen to continue with their characterization and analysis as possible accelerometers/vibrometers and pressure sensors. Some of the selected membranes are listed in Table 3.2 showing both their diameter and their roughness.

Diameter ( $\mu\text{m}$ )	Roughness (nm)
75	5.21
100	7.87
200	9.42
300	6.38
750	8.19

**Table 3.2:** Diameter and roughness of some selected membranes.

From these first results it is possible to conclude that graphene membranes produced with this type of process flow and with the following thermal annealing (section 2.2) are very resistant and can be stored over time. Their performance could degrade but not excessively, continuing to allow their use for different applications.

## Chapter 4

# Accelerometer based on graphene membranes

The device proposed in this section is the evolution of an accelerometer manufactured and characterized previously in the Advanced NEMS Laboratory at EPFL through a study that led to the proof of concept of a graphene-based resonant accelerometer [16]. In fact, a research was performed on accelerometers based on graphene membranes with a silicon mass above, a theory was also developed and completed through the help of some FEM simulations, but a strange effect was noticed at measurements time: the responsivity in resonant frequency shift of the devices due to an applied acceleration was different orders of magnitude higher than expected, not following the trend predicted by the theory. Afterwards, further experiments were done to justify the results obtained. Initially an acceleration was applied to the devices through a piezoshaker varying the intensity of the signal, consequently, a linear shift of the resonance frequency of the membranes was observed, as expected. Subsequently, varying the frequency of the signal to generate an acceleration, the shift no longer followed a linear trend but remained constant. This phenomenon shows that the devices are not accelerometers because they do not detect an acceleration that can be set by a change in amplitude and either by a change in frequency of the signal, but they could be vibrometers or strain sensors, only sensitive to changes in membrane deformation. Several devices with different masses have been tested and all of them showed the same response to acceleration and reported responsivity values close to each other, this led to the hypothesis that there was no need of the mass to observe this phenomenon. For this reason in this part of the project the graphene membranes studied in section 3 are exploited, considering that, having no proof mass, they are the perfect candidates to proceed with this kind of research. So, these membranes are characterized following the steps carried out in the previously mentioned research [16] and then the results are

compared. To further inspect the nature of this phenomenon, that is the shift of the resonance frequency due to a displacement of the membrane, its dependence on the membrane built-in stress is studied. To do so, Taylor expansion of the resonance frequency with respect to the stress is developed. The calculations in detail are reported in the following theory paragraph, however an inversely linear dependence between the relative shift of the resonance frequency, from which device responsivity is derived, and the built-in stress is obtained. In the case of devices with a mass attached to the graphene membrane, the dependence computed is more or less respected. The results are shown in Figure 4.1.

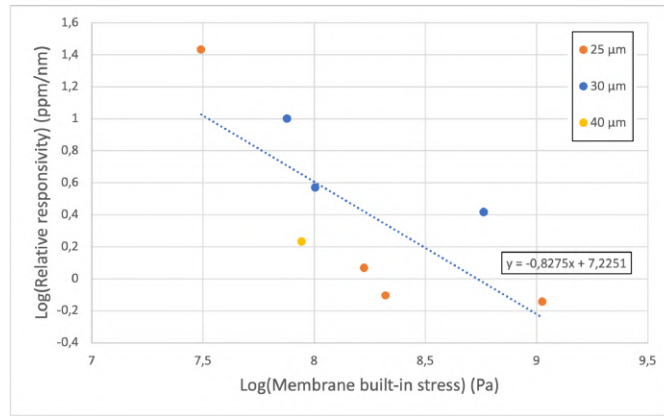


**Figure 4.1:** Results on the dependence of device responsivity due to displacement with respect to membrane built-in stress [36].

The measurements are performed in the study previously cited on graphene membranes with a silicon mass attached [36]. The legend in the graph shows the lengths of one side of the masses, that have square shapes and a height of  $16 \mu\text{m}$ . The dotted line represents the average trend, being the plot in logarithmic scale on both axes, the slope represents the power that binds the two variables, in this case it is very close to -1 as expected. In this project a similar analysis is performed, but considering the membranes without mass to be able to compare the results and see if the same dependence can be observed.

All the steps that have been conducted to properly characterize the graphene membranes are explained in detail in the following paragraphs with a brief introduction on the theory behind these measurements. Moreover, since there are membranes of different diameters available, it can be interesting to conduct a study also based on the size of the membrane that influences the resonance frequency and see if the same effect is noticed on different devices or it is affected by dimensions. The same thing is also done for membranes made of different materials, in particular a comparison with silicon nitride is performed. Therefore, despite many membranes with different diameters have been subjected to the various steps of

the characterization, the detailed explanation of the entire process is made for a single membrane, the comparison of the different results is done only at the end in section 4.6.

## 4.1 Theoretical background

A brief insight on the working principle and on the theory behind the proposed device is given in this paragraph. Firstly, resonant accelerometers are introduced, as they can be considered their precursor. Indeed, such devices aim to be alternatives to those common models that base the detection of a vibration on the motion that is induced on a mass. Alternatives, for some aspects even better, because without the presence of a mass it is easier to decrease the size of the device following the technological trend that distinguishes this era.

### 4.1.1 Model and detection chain

Existing resonant accelerometers can be schematized with a rigid structure to which a mass ( $M$ ) is connected through a spring characterized by an elastic constant ( $k$ ) (Figure 4.2).

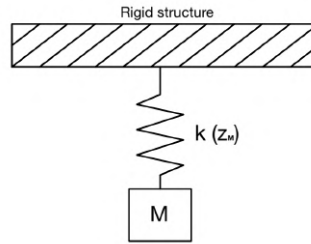


**Figure 4.2:** Model of resonant accelerometer.

Actually, the spring constant stands for the non linear stiffness of the structure that can be tuned through the changing position of the mass. Therefore the acceleration detection comes through the change of stiffness as the applied acceleration generates a force on the mass that determines its displacement. Mass displacement causes an increase of tension in the structure that supports itself and, consequently to this variation of tension the stiffness varies. Since the device is a resonant accelerometer, it is characterized by a certain resonance frequency that depends both on stiffness and mass according to the relation reported in equation 4.1.

$$f_{res} = \sqrt{\frac{k}{M}} \quad (4.1)$$

In all the cases considered in the current analysis, mass is constant, but stiffness, as previously said, can vary, altering the resonance frequency of the device. The detection chain is reported below:

$$a_{ext} \implies F = M \cdot a_{ext} \implies \delta z_M = \frac{F}{k(z_M)} \implies \delta \sigma \implies \delta k(z_M) \implies \delta f_{res} = \sqrt{\frac{\delta k(z_M)}{M}} \quad (4.2)$$

Where  $a$  is the externally applied acceleration,  $F$  is the force that the acceleration generates,  $\delta z_M$  represents the consequent displacement of the mass,  $\delta \sigma$  stands for the change in stress that the structure undergoes,  $\delta k$  is the stiffness variation that indirectly depends on mass position, while  $\delta f_{res}$  is the change of resonance frequency that is detected.

So thanks to these devices it is possible to detect the presence of an acceleration by studying their resonance frequency. Referring to the particular devices proposed in this project, it is necessary to specify the main differences, since the moving mass is no longer present. Nevertheless, the purpose is to try to study their behavior when they are subject to an acceleration and see if it can be noticed a shift in the resonance frequency.

The acceleration, applied through a shaker, can be expressed as the second derivative of the displacement in a harmonic motion (Eq. 4.3).

$$a = \frac{\partial^2 x(t)}{\partial t^2} = \frac{\partial^2 [A \cdot \sin(2\pi f \cdot t)]}{\partial t^2} = -A \cdot (2\pi f)^2 \cdot \sin(2\pi f \cdot t) \quad (4.3)$$

Where  $A$  is the amplitude of the signal sent to the shaker and  $f$  its frequency. Consequently, to apply an acceleration and try to detect the resonance frequency shift, it is possible to act by varying the amplitude of the signal or its frequency. Of course the dependencies are different, a linear increase is observed as the amplitude of the signal increases, while with respect to the frequency the dependence is quadratic (Eq. 4.4).

$$|a| = A \cdot (2\pi f)^2 \quad (4.4)$$

## 4.1.2 Resonant frequencies

Applying an acceleration, the membrane starts to vibrate in a certain way depending on the frequency used. A membrane can vibrate in an endless number of ways, each given by the solutions of the two-dimensional wave equation taking into account some boundary conditions such the circular shape of the membrane and its clamped edges. Each solution is a combination of Bessel functions and can be reduced into a superposition of normal modes of the membrane [37]. A vibrating normal

mode corresponds to a particular shape of the membrane and can be associated with a specific frequency. The normal mode with the lowest frequency is called the fundamental mode. The eigenfrequency of a circular membrane can be easily obtained approximately with the Rayleigh method [38] which leads to equation 4.5.

$$f_{n,j} = \frac{\alpha_{n,j}}{2\pi R} \sqrt{\frac{\sigma}{\rho}} \quad (4.5)$$

Where  $\alpha_{n,j}$  is a constant parameter characteristic of each mode and depends on the number of straight nodal lines  $n$  and of concentric nodal circles  $j$ . While  $R$  is the radius of the membrane,  $\sigma$  is the tensile stress and  $\rho$  the mass density. Some values of  $\alpha_{n,j}$  with their eigenmodes are reported in Figure 4.3.

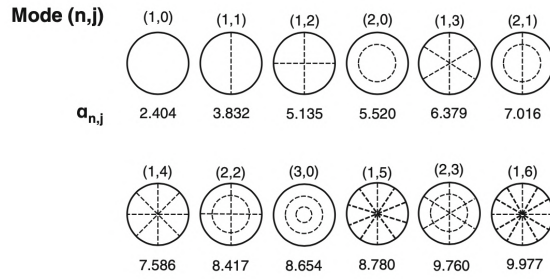


**Figure 4.3:** Eigenmodes and their respective  $\alpha_{n,j}$  values for a circular membrane [38].

Considering equation 4.5 and the values listed in Figure 4.3, the frequency of the fundamental mode for a circular membrane can be computed through the formula 4.6.

$$f_{1,0} = \frac{2,404}{2\pi R} \sqrt{\frac{\sigma}{\rho}} = \frac{4,808}{2\pi D} \sqrt{\frac{\sigma}{\rho}} \quad (4.6)$$

### 4.1.3 Responsivity

To properly characterize a device and understand the quality of its performance, it is necessary to study its responsivity. The term responsivity is referred to the variation of the output of the mechanical resonator with respect to the external stimuli to be measured. In this particular case it is the slope of the resonance frequency shift “ $\partial f_{res}$ ” as a function of the external acceleration “ $a$ ” (Eq. 4.7) and it is expected to be constant over the working range of the sensor.

$$\mathcal{R} = \frac{\partial f_{res}}{\partial a} \quad (4.7)$$

Since the frequency resolution of the resonant frequency is frequently expressed in part per million (ppm), working with relative responsivity is preferable. Additionally,

it can be also convenient in order to have a dependence only on the stimuli. For these reasons responsivity in the following paragraphs is normalized by the resonance frequency (Eq. 4.8).

$$\mathcal{R}_{rel} = \frac{\mathcal{R}}{f_{res}} = \frac{1}{f_{res}} \frac{\partial f_{res}}{\partial a} \quad (4.8)$$

Responsivity can be a reliable parameter to decide the effectiviness and the quality of a sensor, since higher and constant is the responsivity and better are its performances. This should not be confused with sensitivity of a sensor that, instead, describes the minimum detectable variation of the external input parameter with respect to a certain noise level [38].

Knowing the device's responsivity with respect to acceleration and the acceleration frequency, it can be easily calculated also the relative responsivity with respect to the induced displacement in the membrane. It is derived from equations 4.4 and 4.8, obtaining the formula reported in equation 4.9.

$$\mathcal{R}_d = \frac{1}{f_{res}} \frac{\partial f_{res}}{\partial d} \xrightarrow{|d|=\frac{|a|}{\omega^2}} \mathcal{R}_d = \frac{1}{f_{res}} \frac{\partial f_{res}}{\partial \frac{|a|}{\omega^2}} = \mathcal{R}_a \cdot \omega^2 \quad (4.9)$$

It indicates how much the resonance frequency shifts due to a movement of the membrane. Where  $d$  is the displacement,  $a$  is the acceleration,  $R_a$  stands for the relative responsivity computed with respect to acceleration and  $\omega = 2\pi f$  is the frequency of the applied acceleration. Thanks to equation 4.9 the displacement responsivity can be easily derived from the acceleration one, just multiplying twice the latter by the proper frequency.

#### 4.1.4 Built-in stress

As can be noticed from equation 4.6, stress plays a fundamental role in micro and nanomechanical resonators affecting directly their resonant frequency. Each structure has intrinsic stresses, strains and internal forces that generates a preloaded stress, this is called built-in stress and it characterizes each device even before the application of an external stimulus. Such built-in stress can be influenced by many physical causes either during the manufacturing process or during the storage of the device, if it is not carefully controlled and subjected to changes in temperature or pressure.

A Taylor-series expansion of the resonant frequency with respect to the built-in stress of the membrane ( $\sigma_0$ ) is developed to deepen their dependence. It is reported below in equation 4.10 and highlights how a change in built-in stress can affect the resonance frequency of the device and consequently its responsivity.

$$f_{res}(\sigma) = f_{res}(\sigma_0) + \left. \frac{\partial f_{res}}{\partial \sigma} \right|_{\sigma_0} \cdot \delta\sigma \quad (4.10)$$

For the expansion the fundamental resonant frequency is chosen. So considering a circular membrane and the corresponding frequency expressed in equation 4.6, the following formula is obtained:

$$\begin{aligned}
 f_{res}(\sigma) - f_{res}(\sigma_0) &= \frac{4,808}{2\pi D} \frac{1}{2\sqrt{\sigma_0\rho}} \cdot \delta\sigma = \\
 &= \frac{4,808}{2\pi D} \frac{1}{2\sqrt{\sigma_0\rho}} \frac{\sqrt{\sigma_0}}{\sqrt{\sigma_0}} \cdot \delta\sigma = \\
 &= f_{res}(\sigma_0) \cdot \frac{\delta\sigma}{2\sigma_0} = \delta f_{res}
 \end{aligned} \tag{4.11}$$

From equation 4.11 the relation between the relative frequency shift and the built-in stress can be easily derived:

$$\frac{\delta f_{res}}{f_{res}(\sigma_0)} = \frac{\delta\sigma}{2\sigma_0} \tag{4.12}$$

Now it is easy to extract the dependence of the responsivity with respect to built-in stress, in fact it is enough to divide both sides of the equation for the external stimulus that in this case is identified in a displacement of the membrane ( $\delta d$ ). This leads to equation 4.13.

$$\mathcal{R}_d = \frac{\delta f_{res}}{f_{res} \cdot \delta d} = \frac{\delta\sigma}{2\sigma_0 \cdot \delta d} \tag{4.13}$$

As can be seen in equation 4.13, the dependence of responsivity the device is inversely proportional to its built-in stress ( $\mathcal{R}_d \propto \sigma_0^{-1}$ ).

After introducing the main concepts that form the basis of this part of the project, it is possible to continue the dissertation describing the measurements performed and the instruments used.

## 4.2 Measurements set-up

The set-up used for the characterization of graphene membranes consists of three main components: a Laser Doppler Vibrometer (LDV), a vibrometer decoder and a lock-in amplifier. Everything is controlled externally through software interfaces. In particular, an interface is used to place the laser spot directly on the area of interest by moving the LDV objective through very precise piezo-actuators. With the same method it is possible to move the objective also vertically to focus and reach the ideal position, so that the signal reflected by the surface is maximum. Afterwards, there is another software that receives and processes all the data that goes and

comes from the lock-in amplifier, from where the results of the measurements can be acquired and all the parameters regarding the applied accelerations, such as amplitude and frequency, can be set.

The various components are connected to each other as shown in Figure 4.4. The data flow starts from the LDV, where information on tested membranes are captured and sent to the vibrometer decoder. There these last ones are converted to displacements or velocities depending on the option that is selected. In fact, it is possible to choose between obtaining the value of the displacement of the sample or its speed, the choice is based on the frequency that is being considered. For low frequencies it is better to use the data concerning the displacement, while for higher frequencies the velocity. This can be explained through the formulas that bind the maximum displacement amplitude ( $|A_x|$ ) and speed ( $|A_{\dot{x}}|$ ) in a simple harmonic motion with the frequency.

$$x(t) = A \cdot \sin(2\pi f \cdot t) \implies |A_x| = A = \frac{|A_{\dot{x}}|}{2\pi f} \quad (4.14)$$

$$\dot{x}(t) = A \cdot 2\pi f \cdot \cos(2\pi f \cdot t) \implies |A_{\dot{x}}| = 2\pi f \cdot A \quad (4.15)$$

It can be observed that for high frequencies the intensity coming from the displacement signal is lower if compared to the velocity one, because it is attenuated by frequency. As a consequence, velocity measurements at high frequencies are more easily appreciable than that one of displacement, which, instead, is preferable for lower frequencies, especially in the range under the Hz. After conversion, data are read by the lock-in amplifier and displayed on the computer via the LabOne<sup>®</sup> software by Zurich Instrument.

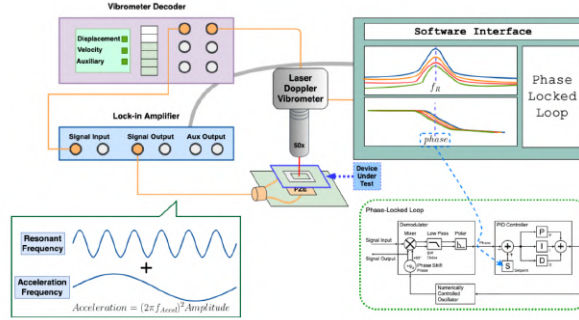


**Figure 4.4:** Complete experimental setup [16].

It is possible to notice how the DUT is pointed by the LDV laser beam and placed over a piezoshaker (PZE), a piezoelectric component that allows to apply an acceleration to the DUT by converting the electric signal provided by the lock-in amplifier into controlled vibrations. These vibrations stimulate the graphene membrane and the study on the shift of their resonant frequency can be performed.

A more detailed explanation of the various steps is given in the following paragraphs, while the description and principle of operation of the main component, the LDV, is given in the subparagraph below.

### 4.2.1 Laser Doppler Vibrometer working principle

The Laser Doppler Vibrometer (LDV) is a very useful device able to measure through a non-contact method the vibrations in a sample. It boasts the best resolution in terms of velocity and displacement detection on the market, allowing measurements down to femtometer within a wide frequency range up to 2 GHz [39]. It is based on an optical set-up similar to the one of the DHM (section 3.2), that incorporates a Mach-Zender interferometer with a "reference beam" and an "object beam" along its two arms.

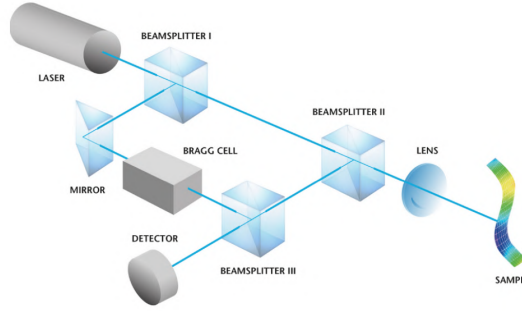


**Figure 4.5:** LDV architecture [39].

The readout principle exploits the Doppler effect, in particular the surface vibrations affect the Doppler frequency of the impinging beam inducing a shift. This beam is reflected back and interferes with the reference one resulting in an intensity modulation at the detector (Fig. 4.5), that leads to the following formula:

$$I_{tot} = I_1 + I_2 + 2 \cdot \sqrt{I_1 \cdot I_2} \cdot \cos\left(2\pi \cdot \frac{r_1 - r_2}{\lambda}\right) \quad (4.16)$$

The total intensity ( $I_{tot}$ ) is composed by the intensities of the two coherent light beams ( $I_1, I_2$ ) that are generated from the laser beam passing through the first beamsplitter, plus the so-called "interference" term, that is directly proportional to their optical path length difference, where  $r_2$  refers to the reference beam and is constant, while  $r_1$  varies according to the movement of the sample creating a light/dark pattern on the detector that stands for constructive (light) or destructive (dark) interference. This term can also be written as a function of the Doppler frequency ( $f_D$ ) whose variation is directly related to the velocity of membrane

vibration as shown in equations 4.17 and 4.18.

$$I_{tot} \propto 2 \cdot \sqrt{I_1 + I_2} \cdot \cos(2\pi \cdot f_D \cdot t) \quad (4.17)$$

$$f_D = 2 \cdot \frac{v}{\lambda} \quad (4.18)$$

Where  $v$  is the sample's velocity and  $\lambda$  is the wavelength of the light source. In this project a He-Ne laser with a wavelength of 632.8 nm is used to perform the measurements, so knowing  $\lambda$  and measuring the frequency shift ( $f_D$ ), it is possible to determine the velocity of the sample's vibrations. Moreover, to determine the direction of the displacement of the sample a Bragg cell is introduced along the reference beam path. This acousto-optic modulator introduces a known frequency shift that generates a precise interference pattern when the sample is at a stationary position. So that an increase or decrease of the modulation frequency will indicate the direction of the displacement of the sample. In this way it is possible to know both the amplitude and the direction of movement. A further merit of the device is that, thanks to its completely optical sensing system, it has no impact on the sample, making it non-invasive and allowing measurements on ultra small and lightweight structures, like the one under test in this project.

## 4.2.2 Measurements under vacuum

Some devices are hard to stimulate through the piezoshaker, this issue can be accounted for by the extremely small membrane dimensions or by damping factors intrinsic of the structure. In these cases, this problem can be overcome by using a vacuum chamber and trying to stimulate the membrane under vacuum. In most cases the problem is solved and the analysis continues with the membrane constantly placed inside the vacuum chamber. In this way it is possible to analyze if vacuum affects the shift of the resonant frequency or if there is no dependence. Considering the possibility of this variation, sometimes a component is added to the complete set-up shown in Figure 4.4. The vacuum chamber is placed firmly under the LDV objective and the piezoshaker is glued inside. To provide the signal to the piezoshaker without altering the vacuum inside the chamber, the connectors in the available model (HFS350EV-PB4 from LINKAM) are used. In particular, one of the four connectors is disassembled and accurately soldered with the piezoshaker. After reassembling the connector, it is possible to provide through it an external signal directly to the piezoshaker.

## 4.3 Measurements for resonant frequency detection

In this paragraph the process to find the resonant frequency of the different membranes is described. It consists in three steps: study of the thermomechanical noise, inspection of device response to a frequency sweep and visualization of membrane displacement through DHM. At the end all the results obtained are summarized and it is possible to derive the built-in stress for each membrane from the corresponding resonance frequency found.

### 4.3.1 Thermomechanical noise study

A first approach to get an idea of the resonance frequency of the membranes consists in analyzing them from a thermomechanical point of view. In fact, pointing with the laser on their surface, heat is transferred and, according to the Fluctuation-Dissipation Theorem, it is transformed into vibrations. A qualitative and intuitive explanation of this phenomenon can be given by seeing dissipation as a passage of energy from the mechanical structure to its thermal environment and viceversa. So, as mechanical energy is transformed into heat during each cycle of vibration when a periodic force is applied to the structure, inversely, the structure will exhibit spontaneous random displacements around its equilibrium position due to an injection of energy from the thermal reservoir (laser) and in absence of any external force [40]. The following is the way the measurements are performed, in particular the setup shown in Figure 4.4 is used, but without turning on the piezoshaker to stimulate the device. The laser excites the membrane, in the meanwhile data are acquired through the LDV and the vibrometer decoder and encoded as velocity time series, then a Fast Fourier transform (FFT) is applied to the entire time series and from the latter the Power Spectral Density (PSD) is calculated, as explained in equation 4.19.

$$\dot{x}(t) \implies \dot{X}(f) \implies S_{\dot{x}} = 2|\dot{X}(f)|^2 \quad (4.19)$$

To get reliable results it is necessary to make first some considerations and set three parameters in the software interface, as shown in Figure 4.6b. These are: the sampling frequency, the number of points to interpolate and the averaging factor. The sampling frequency ( $f_s$ ) is fixed high enough to have a Nyquist frequency ( $0.5f_s$ ) much higher than the resonance frequency of the device. For these measurements a sampling frequency of 880kHz was used, in such a way as to visualize frequencies below 440kHz. The number of points is selected among the available ones and is set to 65536, which is also high to have enough points to well interpolate the curve at the peak of resonance. While, for the averaging factor, it is set to 100 and

represents the range of points to consider during the average that is done to reach the desired signal-to-noise ratio and to reduce the spectral leakage due to FFT.

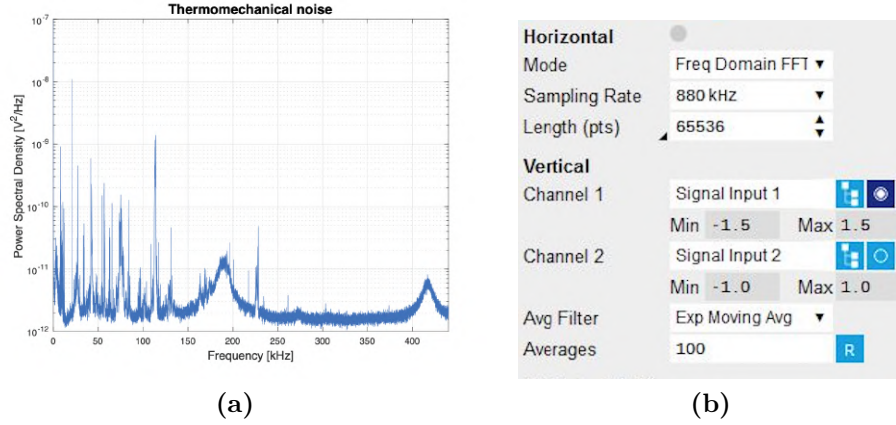


**Figure 4.6:** Thermomechanical noise (a) and parameter setting (b).

The spectrum obtained is shown in Figure 4.6a and it is related to a membrane composed by bilayer graphene and with a diameter of 300 $\mu\text{m}$ . It is possible to notice, besides some peaks at low frequencies due to possible noises of the instrument or building vibrations, a more preponderant peak that should indicate the resonance frequency due to thermomechanical noise. Usually a coarse estimate of this type is sufficient to find the peak of resonance. The other peaks were excluded because trying to repeat the measurement several times and with different parameters their positions were randomic, unlike the one at 193kHz that is always present. Moreover, from the graph it is possible to extract also the level of thermomechanical background noise that is in the order of magnitude of  $10^{-12}\text{V}^2/\text{Hz}$  and that influences all the measures performed with LDV.

### 4.3.2 Frequency sweep response

To confirm the resonance frequency of the device found with the thermomechanical noise, a sweep of the frequency is performed, this time exciting the membrane with the piezoshaker. The latter can be controlled through different driving voltages; higher voltages imply higher displacement of the membrane, as shown in Figure 4.7.

In sweeping through the frequencies it is possible to focus around the frequency range identified during the thermomechanical noise study, neglecting the remaining or at least checking only that there are no significant peaks at other frequencies that have not been highlighted before. So, zooming on 193kHz it is possible to observe a peak that almost follows a gaussian behavior, it is a bit damped on top,

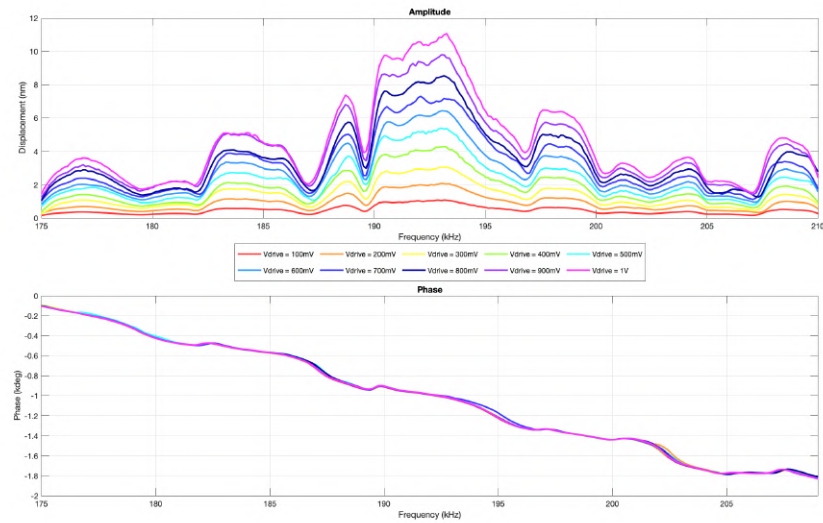


**Figure 4.7:** Response of the device due to a frequency sweep around its resonance peak. The legend reports the different driving voltages applied to the piezoshaker to stimulate the membrane.

but it is plausible because the condition of the membranes under test is not one of the best and some damping factors like the intrinsic one of the material or the one from the presence of sporadic defects and contamination could affect a bit the measure. It is intentionally reported an example far from an ideal resonance peak, to show that although not all the membranes analyzed are in very good condition, it is still possible in most cases to identify a peak along the frequency spectrum.

At this point the voltage that drives the piezoshaker can be increased so as to understand the maximum applicable voltage in order to not damage the membrane and not reach the saturation of the acquisition system, but also to observe if the displacement of the membrane follows the linear increase of the driving voltage or at some point it distorts. For most membranes there is the possibility to push without any problem until reaching the maximum applicable voltage for the instrumentation that is 1.5V, this leads to higher response values and consequently improves measurements by easing the detection of a sample displacement. For example, in Figure 4.7 it can be noticed that the membrane follows the voltage increase deflecting up to about 11 nm in the amplitude's plot, while phase does not change as voltage increases.

### 4.3.3 Membranes displacement through DHM

Once the assumed membrane resonance peak is found, the next step is to determine whether it refers to the fundamental mode or to a higher one. For this verification

the DHM (section 3.2) is used again, this time no longer in static mode but in dynamic mode. In fact, the DHM can be used also in dynamic mode exciting the membrane through a piezoshaker and inspecting its behavior from a mechanical point of view in real time. It is possible also to select between two options of study depending on whether analysis is extended to a range of frequencies or it is limited to a signal with a constant frequency. At this point of the project, since the sweep in frequency is already performed with the LDV, the piezoshaker is excited to vibrate at a fixed frequency, in particular at the frequency that is found previously and is indicated as resonance frequency.

After the first steps of phase and tilt adjustment (section 3.2.2), that are necessary to calibrate the instrument and to determine a reference surface not affected by displacement during the measurements, the DHM is set to stroboscopic mode. First it is performed the 2D visualization of the membrane's profile while it is excited at its resonance frequency. The graph in Figure 4.8 shows the displacement of a central section of the membrane at different intervals of time. From the graph it is possible to see that the deflection of the membrane is symmetrical and perfectly respects what is the fundamental vibrational mode of a circular membrane with a uniform thickness and anchored to a rigid substrate along the perimeter.

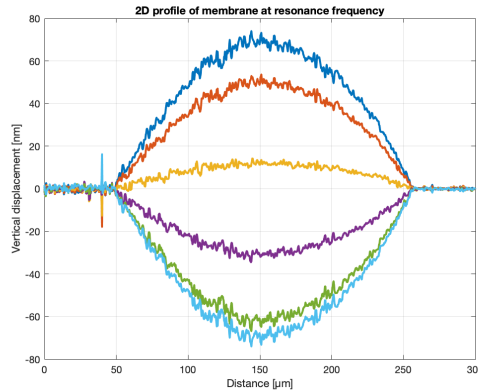


**Figure 4.8:** 2-D profile of the membrane vibrating at its resonant frequency plotted for different time frames.

The vertical displacement reached is about 70 nm. This amplitude is high considering the thickness of the membrane ( $< 1nm$ ) and its diameter ( $200\mu m$ ) and not all the membranes analyzed can reach it. Some membranes are difficult to excite and their maximum displacement stops at a few nanometers in height. The cause can be attributed to defects in the membrane structure or losses due to viscous air damping. For this reason the same study is repeated, but this time inserting the membranes inside a vacuum chamber where pressure is decreased to  $5 \cdot 10^{-4}mbar$ , as described in the subparagraph 4.2.2. In most cases the results

obtained consist of an increase in membrane displacement as expected, as viscous air damping is reduced considerably and the membrane has more freedom to move.

A comparison between a membrane at atmospheric pressure and under vacuum is reported in Figure 4.9.

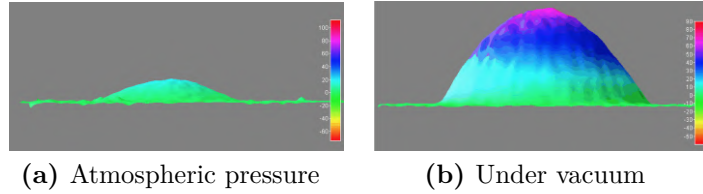


**Figure 4.9:** Comparison between the displacement of the same membrane at atmospheric pressure and under vacuum.

Thanks to DHM, there is the possibility to obtain information on the entire surface of the membrane with a single acquisition and thus reproduce an image of the device, not only in 2-D, but also in 3-D. Moreover, thanks to the high speed of acquisition, it is possible to visualize the hologram of the membrane moving in real time. In Figure 4.10 it is reported an example of the hologram reproduced through the dynamic mode of the DHM and also there it can be noticed as the frequency found with the previous process is that one of the first vibrational mode. This verification is the reason why this further step has been taken.

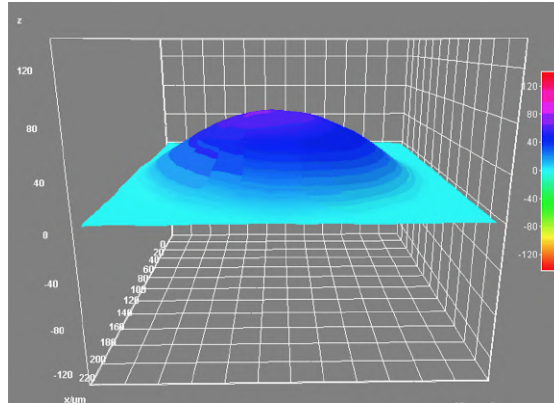


**Figure 4.10:** Frame of the 3-D reproduction in real time of membrane deflection.

#### 4.3.4 Resonant frequency and related built-in stress

After ascertaining that the resonance frequency found is the fundamental one, before proceeding with the application of the acceleration for the study of the

resonance frequency shift, the data collected so far are summarized. These data concern the resonance frequency and are reported in Table 4.1 with the diameter of the corresponding membrane, the related built-in stress and the conditions regarding the pressure at which the measurements are conducted.

Diameter ( $\mu\text{m}$ )	Resonant frequency (Hz)	Built-in stress (Pa)	Pressure condition
750	8.1E+04	1.21E+07	Atmospheric
300	2.06E+05	1.25E+07	Atmospheric
300	1.99E+05	1.16E+07	Atmospheric
200	2.45E+05	7.87E+06	Atmospheric
200	3.92E+05	2.01E+07	Atmospheric
100	3.98E+05	5.20E+06	Atmospheric
100	3.8E+05	4.72E+06	Atmospheric
75	4.03E+05	2.98E+06	Atmospheric
50	3.97E+05	1.29E+06	Atmospheric
50	4.02E+05	1.32E+06	Atmospheric
200	4.11E+05	2.20E+07	Vacuum
100	6.38E+05	1.33E+07	Vacuum
75	1.28E+06	2.98E+07	Vacuum

**Table 4.1:** The four columns contain diameters, resonance frequencies, built-in stress and pressure conditions of the various membranes analysed. In particular the last three lines contain the values of the membranes measured under vacuum.

Pressure conditions may refer to two cases: when measurements are performed at atmospheric pressure (Atmospheric) or when the vacuum chamber is used, with which a pressure of  $5 \cdot 10^{-4} \text{mbar}$  is reached (Vacuum).

For what concerns the built-in stress, it is computed through the inverse function of the fundamental resonance frequency (Eq. 4.6). After simple calculations the following formula is obtained:

$$\sigma_0 = \left( \frac{2\pi f_{res} D}{4,808} \right)^2 \cdot \rho \quad (4.20)$$

Knowing the diameter of the membrane and measuring its resonant frequency, the only missing parameter is the density ( $\rho$ ). The latter is considered uniform over the entire membrane even if this is only an approximation, because, as it is known from the study of membrane surface topography, a variable roughness is present on each device and should contribute to random density variations in some areas of the membrane. However density is derived by multiplying the surface density of graphene, which is equal to  $6.8\text{E-}07 \text{ kg/m}^2$ , by the membrane thickness which in all the cases analyzed in this part of the project corresponds to two layers of carbon atoms, for a total of  $\sim 0.6 \text{ nm}$ .

## 4.4 Acceleration measurement

This paragraph is the fulcrum of this part of the project on accelerometers, in fact, after a first study of the membranes, it moves to the analysis of the phenomenon object of research, that is the detection of the resonance frequency shift due to an external applied acceleration. The acceleration is exerted via a piezoshaker, as shown in Figure 4.4. The device is excited by two signals: a first one oscillating at membrane resonance frequency and a second signal that varies in amplitude or frequency to simulate the effect of an acceleration (Eq. 4.4) and modulates the first one. The variation range is determined before each acquisition and data are recorded for a time interval of 10 seconds for each step of the sweep. Initially, the acquisition time was 60 seconds long, but this resulted in time-consuming waiting period, especially if the same measurements have to be repeated many times on different devices and with large interval sweeps. But it was noticed that results were not altered reducing the acquisition time, therefore a reduced period of 10 seconds was maintained, also because the previous one created files of huge dimensions plenty of useless information. After recording frequency information during the selected time interval (Figure 4.11a), these are processed via a FFT to see the frequency response of the membrane to the applied acceleration. It is expected a modulation of the signal around the acceleration frequency which is intentionally much lower than the resonance frequency. For example in Figure 4.11b it is clearly visible a peak at the acceleration frequency that in this case is 160Hz; this value is chosen since it is often used for the calibration of accelerometers.

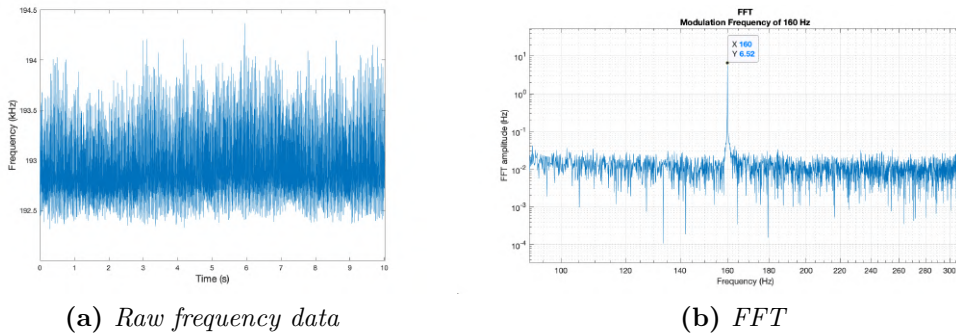


**Figure 4.11:** FFT of frequency data recorded for 10 seconds.

The peak height is given directly in Hz and determines the shift of the resonance frequency specific of that acceleration. For each acceleration used, the same acquisition of the peak height value is repeated from 5 to 10 times, so that an average value can be computed with its respective standard deviation, reducing the error that characterizes each measure and finding the outliers that deviate from

general trend. The various shifts are recorded for different accelerations, but before proceeding with the computation of the corresponding responsivity, a preliminary step has to be performed. This consists in the calibration of the piezoshaker and it is fundamental because permits to associate to each signal sent to the piezoshaker its corresponding acceleration. To do so, the LDV laser is pointed on a flat surface of the device away from the membrane and it is performed the same sweep that is taken into account for the driving voltages or for the frequencies to apply a specific acceleration. The data recorded are then converted to acceleration values according to the type of decoder used choosing between the displacement or the velocity one. Those values are associated to the vibration applied on the entire device and are considered as references for the following measurements that exploit acceleration. The calibration step is performed only once for each device since it is assumed to be characteristic of it, so it is not necessary to repeat it after every measurement. In the graphs of Figure 4.12 two example of calibration are reported.

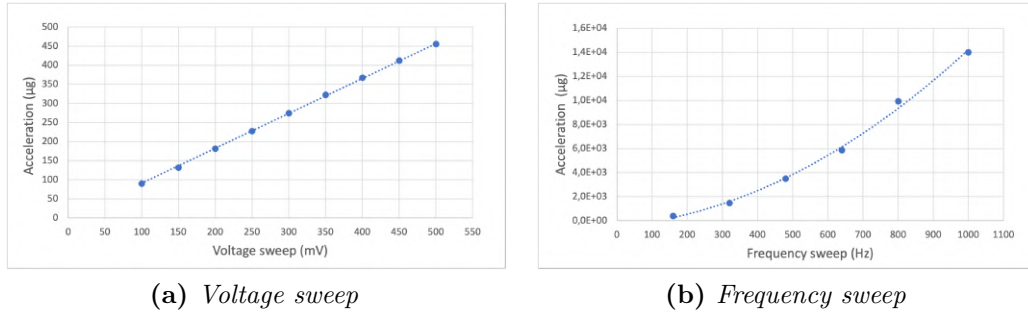


**Figure 4.12:** Calibration of the setup. Measure of provided acceleration due to a sweep in driving voltage and a sweep in frequency. (a) Voltage sweep between 100mV and 500mV with frequency fixed at 160Hz. (b) Frequency sweep between 160Hz and 1000Hz with voltage fixed at 0.5V.

Only one acquisition is done since the measure is quite stable. It is possible to notice (Figure 4.12) how the obtained curves have different dependencies according to the type of parameter swept to generate an acceleration as already shown in equation 4.4. Increasing the driving voltage the signal has a higher amplitude and the acceleration increases linearly with it, while an increase in frequency varies the acceleration quadratically. Another interesting feature that confirms stability and robustness of the calibration is the fact that the data collected perfectly align with their polynomial interpolation, first order with respect to the voltage and second order for the frequency. Moreover they respect the constraint that interpolating curve must cross the origin of the axes, because zero voltage or zero frequency must correspond to zero acceleration.

In the following subparagraphs are reported the measurements performed by

applying the acceleration, first, varying the signal voltage and then only the frequency. The results are analyzed and the study proceeds with the calculation of the corresponding responsivities.

#### 4.4.1 Acceleration due to a change in voltage

The shift of the resonance frequency due to a change in driving voltage is analyzed by setting the acceleration frequency to 160 Hz and performing a sweep between 100 mV and 500 mV with steps of 50 mV. This frequency is chosen because it is far enough from 50 Hz, that is usually the sound noise produced by electronic devices, it is well below the resonance frequency of the membranes and it is one of the one-third octave frequency bands that are used in acoustic measurements. For what concerns the voltage sweep, it is dictated by the limits of the lock-in amplifier that manages to provide a maximum of 1.5V. Since 1V is given to the signal that excites the membrane at its resonance frequency, only 0.5V remains available for the acceleration, but it is enough to obtain appreciable results. Information about the behavior of the resonant frequency for each step of the sweep are collected in data structures through a Matlab script (Appendix A.2) and then are processed obtaining graphs like the one in Figure 4.13.

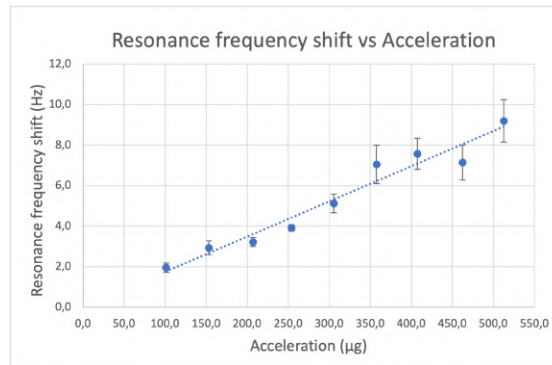


**Figure 4.13:** Shift of the resonant frequency vs Acceleration due to a change in voltage.

It is possible to notice how the shift of the resonance frequency is linear with increasing acceleration resulting in a behavior similar to the one of devices with mass. As a consequence of these results, responsivity is constant and its values are reported in the plot of Figure 4.14.

Actually, what it is computed is the relative responsivity for each acceleration as expressed in equation 4.8. To obtain the final value of responsivity of the device, its mean value and standard error of the mean are computed. The standard error gives the accuracy of the mean value with respect to the true mean and should not be confused with the standard deviation which indicates how accurately the

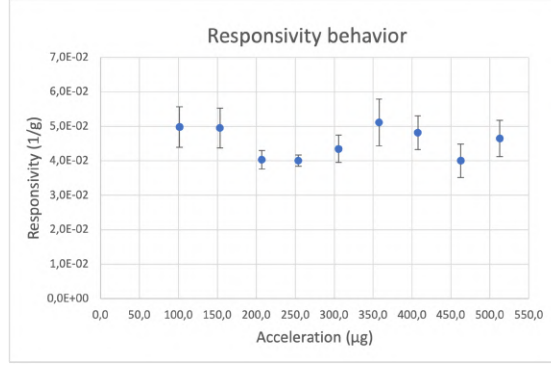


**Figure 4.14:** Responsivity with respect to acceleration due to a change in voltage.

mean represents sample data. It is obtained dividing the standard deviation by the square root of  $N$ , the number of samples, and its precision increases as  $N$  increases [41]. Responsivity mean value comes out of a simple average that takes into account the responsivities for each acceleration (Eq. 4.21), where  $N$  is the number of sweep steps, while for estimating the standard error the formulas from theory of propagation of statistical errors are used (Eq. 4.22), deriving its value from the standard error of the resonance frequency shift ( $\sigma_{\Delta f_{res}}$ ).

$$\bar{\mathcal{R}} = \frac{1}{N} \sum_{i=1}^N \mathcal{R}_i \quad (4.21)$$

$$\begin{aligned} \sigma_{\bar{\mathcal{R}}} &= \frac{\sigma_{\mathcal{R}}}{\sqrt{N}} = \sqrt{\frac{1}{N} \sum_{i=1}^N \left( \frac{\partial \bar{\mathcal{R}}}{\partial \mathcal{R}_i} \right)^2 \sigma_{\mathcal{R}_i}^2} = \sqrt{\frac{1}{N} \sum_{i=1}^N \sigma_{\mathcal{R}_i}^2} = \\ &= \sqrt{\frac{1}{N} \sum_{i=1}^N \left( \frac{\partial \mathcal{R}_i}{\partial (\Delta f_{res_i})} \sigma_{\Delta f_{res_i}} \right)^2} = \sqrt{\frac{1}{N} \sum_{i=1}^N \left( \frac{1}{f_{res_i} a} \sigma_{\Delta f_{res_i}} \right)^2} \end{aligned} \quad (4.22)$$

All the data collected for a membrane of  $100\mu m$  diameter are listed in Table 4.2, where responsivity with its standard error is reported with values of accelerations computed during the calibration step and the corresponding shift. The table is shown to better understand the data available and how they are managed to compute parameter expressed in equations 4.21 and 4.22.

The same measurements and the same data are collected for membranes with different diameter and in all the cases the responsivities obtained are quite high and close to the one of membranes with mass. A more detailed comparison is performed in section 4.6.

Diameter ( $\mu\text{m}$ )	100									
Resonant freq $f_{res}$ (kHz)	385.72									
Vsweep (mV)	100	150	200	250	300	350	400	450	500	
Acceleration $a$ ( $\mu\text{g}$ )	1.01E+2	1.53E+2	2.07E+2	2.54E+2	3.06E+2	3.58E+2	4.07E+2	4.62E+2	5.13E+2	
Resonant freq shift $\Delta f_{resi}$ (Hz)	1.95E+0	2.93E+0	3.22E+0	3.92E+0	5.12E+0	7.05E+0	7.57E+0	7.14E+0	9.19E+0	
St. Err $\sigma_{\Delta f_{resi}}$ (Hz)	2.29E-1	3.42E-1	2.16E-1	1.57E-1	4.70E-1	9.43E-1	7.69E-1	8.70E-1	1.04E+0	
Responsivity $\bar{\mathcal{R}}$ (1/g)	4.98E-2	4.95E-2	4.03E-2	4.00E-2	4.35E-2	5.11E-2	4.81E-2	4.00E-2	4.65E-2	4.54E-2
St. Err $\sigma_{\bar{\mathcal{R}}}$ (1/g)	5.87E-3	5.78E-3	2.71E-3	1.60E-3	3.99E-3	6.84E-3	4.89E-3	4.88E-3	5.28E-3	4.90E-3

**Table 4.2:** Data of a  $100\mu\text{m}$  membrane with a resonance frequency of 386 kHz. Voltage sweep and the corresponding acceleration are obtained from calibration step. Resonant frequency shift is the result of average of 5 independent measurements from which the standard error can also be derived. Responsivity of the device and its standard error are located at the bottom right of the last two rows and are obtained through the equations 4.21 and 4.22.

#### 4.4.2 Acceleration due to a change in frequency

Until now, measurements have led to results similar to those expected with a shift in the resonance frequency as the acceleration changes. Now the study proceeds with the inspection of membranes behavior when subjected to accelerations produced by signals with the same voltage, but with different frequencies and see if the same effect obtained previously can be noticed or if the resonance frequency remains constant as in the case of the membranes with mass.

To apply the desired accelerations with different frequencies another Matlab script is used, it is very similar to one for voltage sweep reported in Appendix A.2. As previously done, firstly the parameters of the main signal are set, with amplitude equal to 1V, while frequency is the resonance one. Instead for what concerns the modulating signal, amplitude is set to the maximum permitted, that is 0.5V, while frequency, the parameter that introduces the acceleration, is let varying within an interval ranging from 160Hz to 1000Hz with steps that more or less follow the one-third octave bands to uniformly cover the frequency range.

The obtained results are reported with their corresponding standard errors in Figure 4.15.

How it is possible to observe, increasing the acceleration provided by the piezoshaker the shift of the resonant frequency remains constant. The effect is the same as the one observed in membranes with mass, so the responsivity is expected to be the same, decreasing for higher accelerations. As already done for acceleration generated by a voltage variation, the responsivity is calculated for each step of the frequency sweep and plotted in Figure 4.16. Acceleration values obtained through the calibration step are considered.

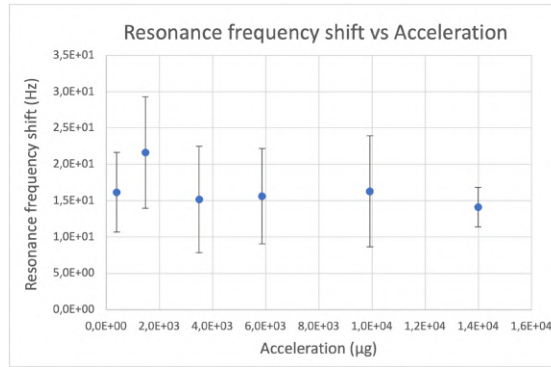


**Figure 4.15:** Shift of the resonant frequency vs Acceleration due to a change in frequency.

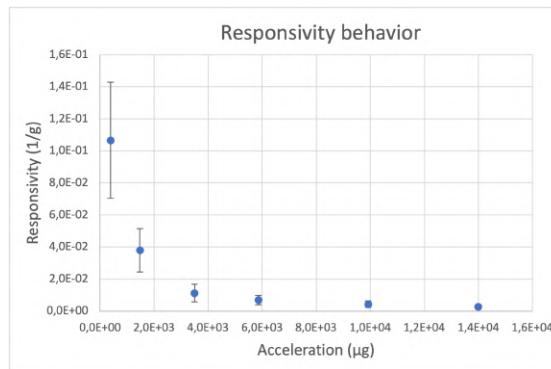


**Figure 4.16:** Responsivity with respect to acceleration due to a change in voltage.

The behavior of the responsivity turns out to be decreasing with the increase of the acceleration. In particular, its trend seems to follow the sweep of the frequencies that generate the acceleration with a proportion of  $f^{-2}$ . The same results are obtained for each membrane analyzed suggesting an insensitivity of the device to acceleration.

An example of data collected through the study of the device resonance frequency when subjected to an acceleration due to a change in frequency is given in Table 4.3. The reported case is the one of the same membrane with a diameter of  $100\mu m$  also used in the previous subparagraph.

<b>Diameter</b> ( $\mu\text{m}$ )	100						
<b>Resonant freq</b> $f_{res}$ (kHz)	385.72						
<b>Fsweep</b> (Hz)	160	320	480	640	800	1000	
<b>Acceleration</b> $a$ ( $\mu\text{g}$ )	3.93E+2	1.47E+3	3.50E+3	5.86E+3	9.92E+3	1.40E+4	
<b>Resonant freq shift</b> $\Delta f_{res_i}$ (Hz)	1.62E+1	2.16E+1	1.52E+1	1.56E+1	1.63E+1	1.41E+1	
<b>St. Err</b> $\sigma_{\Delta f_{res_i}}$ (Hz)	5.48E+0	7.67E+0	7.32E+0	6.57E+0	7.62E+0	2.72E+0	
<b>Responsivity</b> $\bar{\mathcal{R}}$ (1/g)	1.07E-1	3.81E-2	1.13E-2	6.91E-3	4.26E-3	2.62E-3	2.83E-2
<b>St. Err</b> $\sigma_{\bar{\mathcal{R}}}$ (1/g)	3.61E-2	1.35E-2	5.43E-3	2.91E-3	1.99E-3	5.05E-4	1.60E-2

**Table 4.3:** Data of a  $100\mu\text{m}$  membrane with a resonance frequency of 386 kHz. Frequency sweep and the corresponding acceleration are obtained from calibration step. Resonant frequency shift is the result of average of 5 independent measurements from which the standard error can also be derived. Responsivity of the device and its standard error are located at the bottom right of the last two rows and are obtained through the equations 4.21 and 4.22.

### 4.4.3 Responsivity with respect to displacement

Comparing the responsivities for both sweeps it is noticed that if we refer to the acceleration in the case of the sweep in frequency, it decreases quadratically, while this does not happen for the voltage sweep. This mismatch shows that even in the studied case, where the devices are simple membranes without any suspended mass, they are not sensitive to acceleration, but to displacement. In fact, the phenomenon observed is the same in several devices and the position is the only parameter whose amplitude does not depend on frequency, but only on the voltage applied (Eq. 4.14), unlike speed 4.15 and acceleration 4.3. Since these devices appear to be sensitive to a change in membrane position, it is more useful and reasonable to calculate responsivity not as a function of acceleration, but of displacement. For this reason the new responsivity ( $\mathcal{R}_d$ ) is calculated with respect to displacement following the formula obtained in equation 4.9.

An example of the obtained results due to both frequency and voltage sweeps is reported in Figure 4.17, where it can be noted that, considering displacement responsivity, it is constant for both variations with also very similar values.

These data demonstrate that devices are reliable from this new point of view and could further confirm that the origin of the shift comes from membrane displacement.

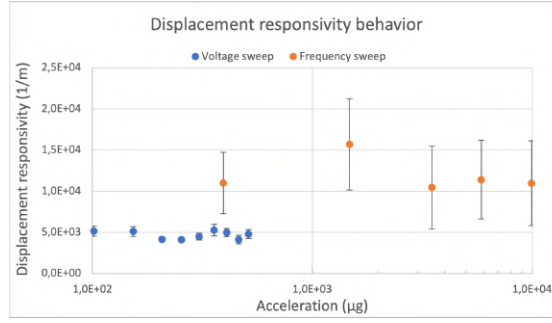


**Figure 4.17:** Displacement responsivity behavior. Voltage sweep between 100mV and 500mV at a constant frequency equal to 160Hz. Frequency sweep between 160Hz and 1000Hz at a constant driving voltage equal to 500mV.

## 4.5 Measurements reproduced on different devices

Slightly different devices are introduced in this section, which are subjected to the same measurements as the graphene membranes proposed in this study, in order to compare their results with the one already obtained and conduct a more complete analysis.

### 4.5.1 Comparison with 30 μm membrane

In order to better inspect the phenomenon under study, a comparison is made with other graphene membranes to check if the same effect can be observed on devices that have been manufactured more recently and have no defects or at most very few, so with a better surface condition both at cleaning level, either structurally. These membranes were fabricated by the Division of Micro and Nanosystems at KTH in Sweden, they have the same structure of the devices analyzed so far, circular membranes clamped at their edges; the only difference is their diameter which is smaller and equal to 30 μm. Having these membranes available it is possible to repeat the same steps from thermomechanical noise up to the study of the resonance frequency shift and compare the results with those already obtained. The only problem is that being very small membranes it is difficult to stimulate them through the piezoshaker, so to facilitate their movement reducing the viscous damping, they are inserted in the vacuum chamber and pressure is decreased to  $5 \cdot 10^{-4} \text{ mbar}$  exploiting the set-up described in subparagraph 4.2.2. In this way it is easier to detect the resonant peak of the membrane and proceed with the analysis. To develop a consistent discussion, being performed under vacuum, the measurements are compared with the other one which are conducted at the same conditions and exploit the vacuum chamber.

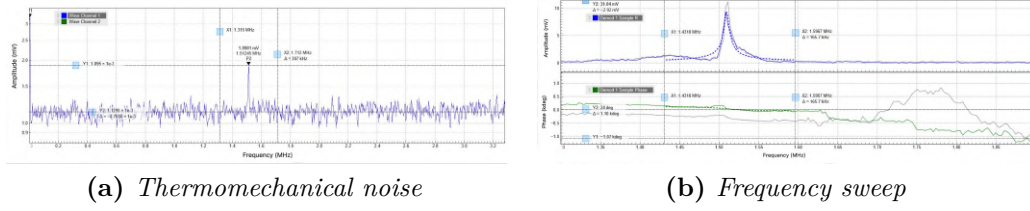


**Figure 4.18:** Study on the  $30\mu\text{m}$  diameter membrane with a resonance peak at 1.51 MHz. a) Thermomechanical noise is plotted in V, but the Power spectral density can be easily derived. b) Sweep in frequency is performed and a peak at the same frequency of the one in TMN is detected.

It can be noticed that graphs in Figure 4.18 are much cleaner and without noisy peaks that disturb the signal. This is derived by the cleanliness and the better surface condition of the device. In both cases a single peak at the same frequency of 1.5MHz is clearly distinguishable and corresponds to membrane resonant frequency. This frequency is much higher than other membranes, but this is justifiable by the fact that the diameter of the membrane is much smaller and the measurements are performed under vacuum, condition that further increases the resonance frequency [42]. The exploited improved quality of graphene should lead to more reliable results in the resonance frequency shift analysis. These are measured and reported in Figure 4.19.

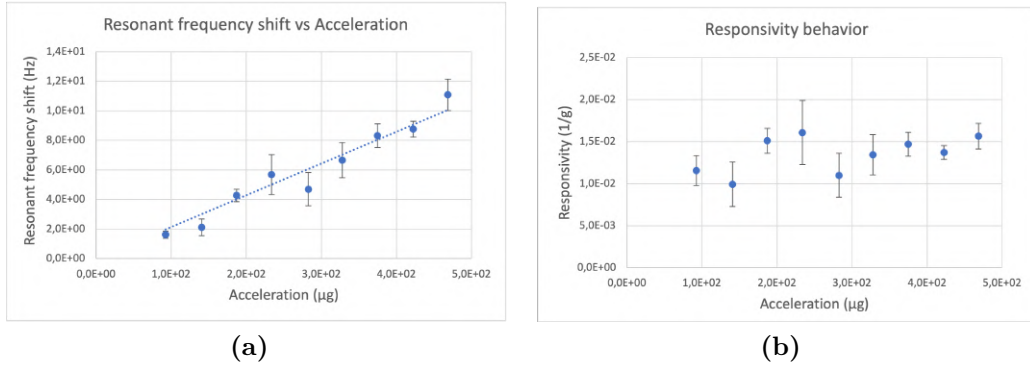


**Figure 4.19:** Shift of the resonant frequency vs Acceleration due to a change in voltage for the  $30\mu\text{m}$  membrane and responsivity for each acceleration.

Looking at the results, also in this device it can be noticed a behavior very similar to that one of other membranes, showing that despite the not optimal conditions of the previous graphene surfaces, the observed phenomenon is visible in every device.

The main parameters characterizing the analyzed devices are shown in Table 4.4. Both responsivities are reported with the corresponding standard errors, but only

that one with respect to the displacement is taken into account in the subsequent comparison, considering that the same result as for the previous membranes are obtained with insensitivity to acceleration due to a change in frequency. Moreover, built-in stress is also derived from the resonance frequency and comparing it with the stress of other membranes analyzed under vacuum, it is possible to observe a slightly lower value due to the fact that the membrane has better surface condition.

Diameter ( $\mu\text{m}$ )	Resonant frequency (kHz)	Accel responsivity (1/g)	Accel responsivity St.Err (1/g)	Displ responsivity (1/m)	Displ responsivity St.Err (1/m)	Built-in stress (Pa)
30	1510	1.35E-2	2.23E-3	1.39E+3	2.29E+2	6.7E+6

**Table 4.4:** Data of 30  $\mu\text{m}$  diameter graphene membrane.

## 4.5.2 Comparison with SiN membranes

Another meaningful comparison is performed with membranes made of a different material, in particular, silicon nitride is used instead of graphene. Such material, thanks to its excellent mechanical properties, has attracted attention for the fabrication of highly resistant suspended membranes [43]. The available devices are provided by Miraex, a startup from EPFL Innovation Park that deals with sensors. The structure of these devices is very similar to that one of the devices analyzed in this project, as it consists of suspended membranes, the only structural difference is that they have a square shape with a side long 1.3 mm. Originally they were to be used as pressure sensors, but in this case they are characterized with the same steps described in the previous paragraphs to see if the same phenomenon can be observed.

The resonance frequency of these membranes is found to be 173kHz. The resonance peak is always determined following the same procedure, starting with the thermomechanical noise and continuing with the sweep in frequencies stimulating the membrane with the piezoshaker. Afterwards, applying the acceleration through the second signal with a lower frequency and varying its amplitude was noted a pattern very similar to that of graphene membranes, in fact it is possible to observe a linear shift of the resonance frequency and a corresponding constant responsivity, as shown in Figure 4.20.

The analysis proceeds providing the acceleration due to a change in the signal frequency to observe if the same phenomenon can be seen, but the results follows the behavior of previous devices with a zero resonance frequency shift and a consequent decrease of the responsivity as acceleration increases.

Therefore, observing the measurements reported in Figures 4.20 and 4.21, it is possible to conclude that, even in this case, the membrane is sensitive to vibrations and not to accelerations. As already done for graphene membranes, the displacement responsivity with the corresponding standard error are computed and listed in

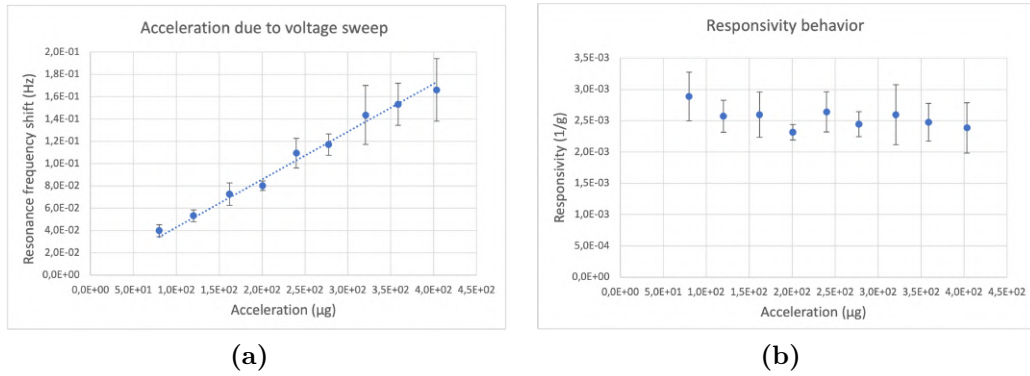


**Figure 4.20:** SiN membrane resonance frequency shift and responsivity due to acceleration (voltage sweep between 100mV and 500mV, frequency fixed to 160Hz).

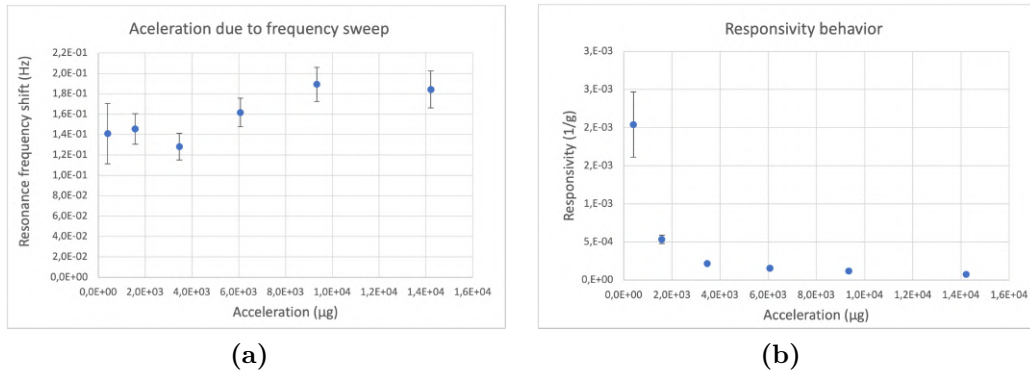


**Figure 4.21:** SiN membrane resonance frequency shift and responsivity due to acceleration (frequency sweep between 160Hz and 1000Hz, voltage fixed to 0.5V).

Table 4.5. In the same table also the membrane built-in stress is reported. For what concerns this device, it is not derived from the resonance frequency, since is known by suppliers and equal to 160 MPa.

Resonant frequency (kHz)	Accel responsivity (1/g)	Accel responsivity St.Err (1/g)	Displ responsivity (1/m)	Displ responsivity St.Err (1/m)	Built-in stress (Pa)
173	2.55E-3	3.31E-4	2.63E+2	3.42E+1	1.6E+8

**Table 4.5:** Data of silicon nitride membrane.

## **4.6 Discussion**

### **4.6.1 Detection of vibrations**

The experiments showed the same phenomenon in all the devices analyzed. In detail, the resonance frequency shift is detected only when the driving voltage of the signal applied to the piezoshaker varies and not when its frequency changes, as observed in devices composed by the graphene membrane with a mass attached. So, it is possible to conclude that this shift is caused by vibrations and it is not sensitive to accelerations. More precisely, a possible solution, which is proposed, is that vibrations cause membrane displacement, thereafter, changing the amplitude of the external stimulus, more and more displacement is generated, with a consequent change in stress of the membrane. The same experiments are conducted under vacuum and with membranes of SiN. In particular, vacuum measurements are performed to see if the same effect can be detected even at those pressure conditions or if it could even be amplified, but the results show that the improvement is not very noticeable, as can be seen in Table 4.4 for a 30 $\mu$ m diameter membrane. Therefore the phenomenon is not affected by the presence or absence of vacuum and future studies or application can continue at atmospheric pressure. While, for what concerns the type of material, even with silicon nitride the same phenomenon is visible, but the responsivity obtained is lower than that of graphene, as listed in Table 4.5, for this reason graphene membrane are preferable. A prospective application for these devices, not being able to be exploited as accelerometers, can be the realization of a strain sensor or a vibrometer based on the detection of the resonance frequency shift and able to detect also extremely small vibrations thanks to the high responsivity measured for some devices. These responsivity values can be attributed to the unique properties of graphene and allow to detect movements with a sensitivity even below nanometers, opening the door to new applications.

### **4.6.2 Possibility to remove the mass**

Another meaningful result is the confirmation that the mass attached to membrane is not needed, considering that the same results can be obtained even without. There are pros and cons in avoiding the use of a mass because if on one side the devices are easier to fabricate not having to attach a mass to the membrane, on the other side it could be harder to attenuate the membrane, as the mass facilitates its displacement. However, this discovery is very useful because by sacrificing the mass it is possible to significantly reduce the size of the device and at the same time maintain almost the same responsivity. Moreover, it aligns with the technology trend described in Chapter 1, that provides for a continuous miniaturization of devices. A comparison between the two devices with and without mass is performed,

adding the results obtained to the one already reported in Figure 4.1. Also in this case the responsivity is plotted in function of the built-in stress to inspect its influence on device performance. Data are shown in Figure 4.22 where the interpolating lines are added in order to delineate the trend of the two distributions and observe if they follow the theoretical relation derived in subparagraph 4.1.4 and expressed in equation 4.13.

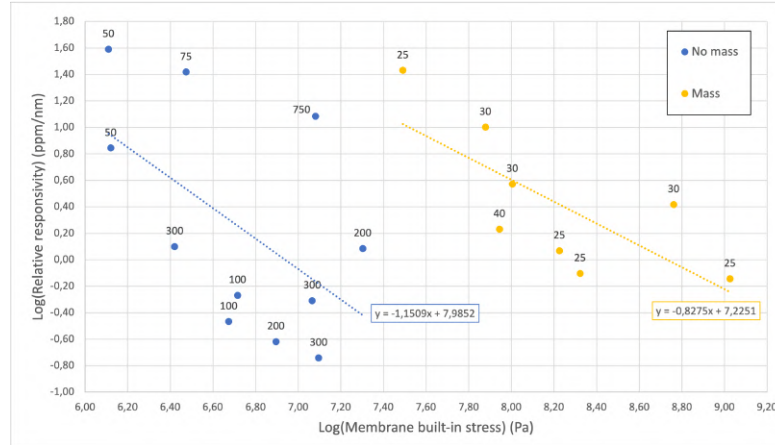


**Figure 4.22:** Relative displacement responsivity vs membrane built-in stress. The mass-free membrane data are reported in blue (No mass) and are identified through their diameter in micrometers, while the membranes with the mass attached are in yellow (Mass) and the their label indicates the length of one side of the mass in micrometers.

The predicted relation between the two parameters ( $\mathcal{R}_d \propto \sigma_0^{-1}$ ) can be confirmed also by measurements on membranes without mass, obtaining a decreasing behavior of responsivity due to an increase of the built-in stress. Comparing both devices, it can be noticed as they have almost the same responsivity, but different built-in stress. This mismatch can be justified by the presence of the mass that introduces an extra contribution to the stress of the membrane. Theoretically following the interpolating curve, devices with mass should have a better responsivity under the same built-in stress, but this has to be considered during the manufacturing process, trying to reduce the stress and see the results in responsivity.

It is also interesting to point out how the slope of the interpolating curves for both type of devices is close to -1 (Figure 4.22), that stands for the power that binds responsivity and built-in stress being the plot in logarithmic scale on both axis.

### 4.6.3 Dependence on dimensions and material

Focusing on graphene membranes without mass and referring to the graph in Figure 4.22, it is not possible to clearly distinguish a dependence on the size of the

membrane. In fact, characterizing several membranes with different diameters the results almost follow the predicted curve and alternate randomly depending on the diameter. To have a better perception of the analyzed values they are listed in Table 4.6, where both displacement responsivity and built-in stress are listed for different membrane diameters.

Diameter ( $\mu\text{m}$ )	Displ responsivity ( $1/\text{m}$ )	Displ responsivity Standard Error ( $1/\text{m}$ )	Built-in stress (Pa)
750	1.22E+04	1.66E+03	1.21E+07
300	1.82E+02	2.80E+01	1.25E+07
300	4.92E+02	4.60E+01	1.16E+07
300	1.26E+03	2.01E+02	2.63E+06
200	2.41E+02	8.08E+01	7.87E+06
200	1.22E+03	5.26E+02	2.01E+07
100	5.38E+02	6.86E+01	5.20E+06
100	3.41E+02	7.21E+01	4.72E+06
75	2.62E+04	1.00E+04	2.98E+06
50	3.90E+04	1.10E+04	1.29E+06
50	6.99E+03	2.29E+03	1.32E+06

**Table 4.6:** Data of graphene membranes without mass.

Proceeding with the analysis of the possible dependence of the phenomenon analyzed and referring to the relationship between responsivity and built-in stress it is possible to notice how the data collected for the membranes in silicon nitride align with what is the trend predicted by the theory, in fact, having a built-in stress greater than the graphene membranes, they result in a lower displacement responsivity. In this way it is possible to explain the poor responsivity value measured in these devices. It might be interesting to try to fabricate SiN membranes with a lower built-in stress similar to that of graphene and measure the responsivity to see if it increases and reaches that of graphene or if it remains lower.

#### 4.6.4 Possible future improvements of the measurements

Nevertheless, it is important to remember that the measures performed are affected by uncertainty and these could hide some dependency. For what concerns responsivity, its standard error is evidently shown in Figure 4.23.

It is interesting to note how the interpolating curve is very close to the theoretical one with a slope of -1. But the low accuracy in the computation of built-in stress has to be always taken into account. Indeed, a constant density over the entire surface is assumed, but this assumption is not true in most cases. As explained in Chapter 3, each membrane has its own roughness that cannot be removed and, in addition, it could be affected by contaminants or structural defects. All these factors directly influence surface density adding an extra mass that is not taken

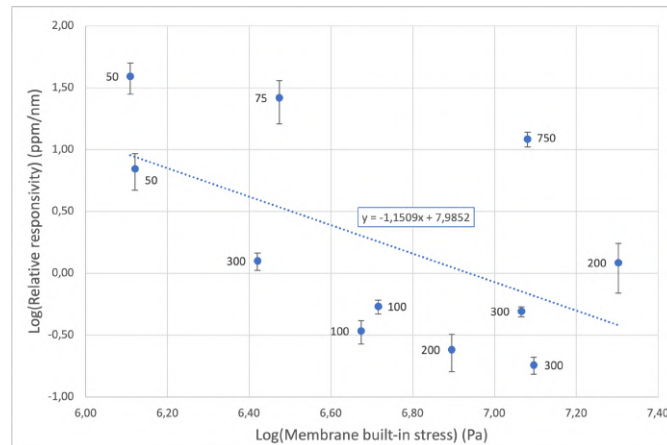


**Figure 4.23:** Zoom in of relative displacement responsivity vs membrane built-in stress for membranes without mass with a focus on standard errors.

into account. Even a small change in density is propagated to the built-in stress, as it is computed through the inverse formula of the resonance frequency (Eq. 4.20). Consequently a small error in surface mass can easily propagate to stress value and could deviate the correct results closer or farther from predicted behavior. But despite these errors, a slightly alignment with theory can be observed.

To reduce uncertainties in measurements it would be necessary to fabricate each device under the same condition and in an automatized way. In that way the resulted membranes should have almost the same surface conditions and further improving the manufacturing process and conservation it would be possible to reach and maintain low roughness values. A continuation of this project could be the re-fabrication of the same device described in Chapter 2.1 trying to obtain better results and repeat the same measurements on the new membranes. This could be time-consuming, as the fabrication of these devices is a very delicate process and it is difficult to obtain good results over a wide range of samples, but it could help in this research leading to more reliable results.

Another scenario to explore could be the study of how the responsivity of the device can be improved, perhaps reducing the built-in stress or setting up a more stable system for measurement and attenuation of the membrane.

Moreover, considering that the readout system is based on optics and interference of laser beams, the presence of electronic components is not expected except at distance, therefore it would be insensitive to electromagnetic disturbances that could alter the measurements. In conclusion, combining all the features of these devices, they would lead to the realization of super miniaturized and super sensitive sensors with different applications from the biomedical field to the Iot, up to measurements that require extreme precision.

## Chapter 5

# Pressure sensor based on graphene membranes

A second possible application of the graphene membranes under study is proposed in this chapter. In fact, these could be used as pressure sensors and be integrated into a microphone. In particular, the microphone proposed wants to take advantage of the peculiar thickness of graphene ( $\sim 0.355nm$ ) and the possibility of having membranes with a fairly large diameter ( $> 300\mu m$ ) to theoretically obtain devices with a very high responsivity and with a wide bandwidth, able to go up to ultrasound. Moreover, a fully optical read-out mechanism is proposed to allow its application in harsh environments, withstanding high temperatures and without the measurements being compromised by possible electromagnetic disturbances as the electronic components used can be placed remotely from the location of the measurements and the signal is transmitted optically. Afterwards, starting from one of the membranes selected by the process described in Chapter 3, a potential packaging of the device is studied, this involves the installation of the optical fiber on the back of the membrane to measure its displacement and the introduction of a rigid structure in such a way as to facilitate the handling of the device. In the first paragraph the working principle of the microphone is described, this is followed by a paragraph on how the optical fiber is placed near the membrane, then, in the third one the measurements made to characterize the microphone are described and in the last paragraph the results obtained are commented and solutions to the problems encountered are proposed. This part of the project is carried out in collaboration with Miraex, a startup of EPFL Innovation Park.

## 5.1 Working principle

The working principle of the microphone is based on the detection by an optical signal of the force that an acoustic wave exerts on the graphene membrane. This force deflects the membrane and consequently influences the optical path of the reflected signal, which can be modulated in intensity, phase or polarization. In the case reported in this project modulation is based on intensity. This choice is made for the sake of simplicity both from an instrumentation and a stability point of view. Exploiting intensity modulation it is possible to use just a photodiode to transduce the optical signal into an electric one, since it is directly sensitive to the intensity of the reflected light beam and there is no need of extra components like an interferometer or a polarizer to control respectively phase or polarization of the wave. In addition, with this type of modulation the read-out system is more stable than one based on interference. The light beam incident on the graphene diaphragm is reflected back towards the photodiode, a movement of the membrane involves a change in its optical path and a consequent variation of its associated optical power, which directly modulates the intensity of the beam.

After classifying the modulation principle, it has to be described the transduction chain to switch from acoustic wave to electrical signal. There are three stages in which the transduction from one energy domain to another takes place. The first one is the acousto-mechanical stage where transition from acoustic domain to mechanical one is performed, thanks to the displacement of the membrane caused by the pressure exerted by the acoustic wave. After that, from mechanical domain to the optical one there is the mechano-optical stage that includes the change in coupled optical power into the fiber due to mechanical displacement of the membrane. Finally, the last transduction stage is the opto-electrical one that is composed by one or more photodiodes that convert coupled power of the optical signal into an electrical signal.

### 5.1.1 Responsivity

Responsivity to an external stimulus is studied also for this device. Each transduction stage has its own responsivity that corresponds to the change in output related to a change in input. The overall responsivity of the microphone is calculated by multiplying the three responsivities and is measured in  $\frac{V}{Pa}$ , that is the amount of voltage measured given a certain acoustic wave pressure. Responsivities of the individual stages are listed below [44]:

- Acousto-mechanical stage responsivity: ratio between displacement ( $z$ ) of the membrane and externally applied acoustic pressure ( $P$ ). It is measured in  $\frac{m}{Pa}$

and is expressed through equation 5.1.

$$\mathcal{R}_{am} = \frac{\partial z}{\partial P} \quad (5.1)$$

- Mechano-optical stage responsivity: ratio between the variations in coupling factor ( $\eta$ ) between output and input fiber optical power and the change in length of the gap ( $g$ ) between the membrane and the end of the optic fiber. It is measured in  $\frac{W/W}{m}$  and is expressed through equation 5.2.

$$\mathcal{R}_{mo} = \frac{\partial \eta}{\partial g} \quad (5.2)$$

Where  $\eta$  is the ratio between the modulated power, reflected by the membrane, and the input power from the fiber.

- Opto-electrical stage responsivity: ratio between the voltage ( $V$ ) measured at the output of the photodetector and the coupled optical power that arrives at its input. It depends on the quality of the photodiode used. It is measured in  $\frac{V}{W/W}$  and is expressed through equation 5.3.

$$\mathcal{R}_{oe} = \frac{\partial V}{\partial \eta} \quad (5.3)$$

### 5.1.2 Responsivity optimization

To try to achieve better performance, the goal of this part of the project is to study how to maximize responsivity. There are different ways to optimize the responsivity of the microphone. Above all, since the special feature of this microphone is the use of graphene membranes, it is interesting to see how the responsivity of the acousto-mechanical stage can be improved. For this reason its dependencies are investigated, starting from the amplitude response to a force of a resonator [38], expressed in equation 5.4.

$$z(\omega) = \frac{1/m}{\sqrt{(\omega_0^2 - \omega^2)^2 + \frac{\omega_0^2 \cdot \omega^2}{Q^2}}} \cdot F \quad (5.4)$$

Where  $m$  is the mass of the resonator,  $\omega_0$  stands for its fundamental frequency,  $Q$  is the quality factor and  $F$  is the applied force.

The equation 5.4 can be contextualized and expressed with respect to the membrane under study. After some calculations, changing the force into pressure

( $F = P \cdot 2\pi R^2$ ) and approximating the fundamental frequency to the one of a circular membrane ( $\omega_0 \approx \frac{1}{R}\sqrt{\frac{\sigma}{\rho}}$ , see Eq. 4.6), equation 5.5 is obtained.

$$z(\omega) = \frac{P \cdot 2\pi R^2}{\frac{m \cdot \sigma}{R^2 \cdot \rho} \sqrt{\left(1 - \left(\frac{\omega}{\omega_0}\right)^2\right)^2 + \left(\frac{\omega}{Q \cdot \omega_0}\right)^2}} = \frac{P \cdot R^2}{\sigma \cdot t \cdot \sqrt{\left(1 - \left(\frac{\omega}{\omega_0}\right)^2\right)^2 + \left(\frac{\omega}{Q \cdot \omega_0}\right)^2}} \quad (5.5)$$

Where  $\rho$  is the density of the membrane,  $\sigma$  is its stress,  $R$  represents the radius and  $t$  the thickness of the membrane, while  $P$  is the acoustic pressure. Deriving equation 5.5 with respect to pressure, as expressed in equation 5.1, responsivity of the acousto-mechanical stage is obtained (Eq. 5.6).

$$\mathcal{R}_{am} = \frac{R^2}{\sigma \cdot t} \frac{1}{\sqrt{\left(1 - \left(\frac{\omega}{\omega_0}\right)^2\right)^2 + \left(\frac{\omega}{Q \cdot \omega_0}\right)^2}} \quad (5.6)$$

As can be noticed the responsivity is directly proportional to the radius of the membrane and inversely proportional to its thickness, so it is possible to optimize the responsivity of this stage acting on the geometrical parameter of the membrane. The use of graphene for the realization of these membranes maximizes the responsivity, because the thickness of the diaphragm can be the minimum physically attainable if the exploited graphene is the monolayer one.

In addition to the size, responsivity also depends on frequency. The relation between responsivity and frequency of the incoming acoustic wave can be seen in Figure 5.1, where it is shown how an increase of membrane aspect ratio (AR) directly increases responsivity and, at the same time, its value is kept constant also for higher frequency as the number of graphene layer decreases.

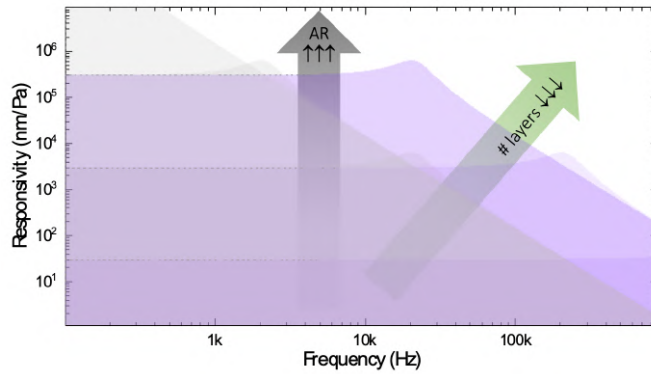


**Figure 5.1:** Microphone diaphragm responsivity vs Frequency with an highlight on geometrical dependencies.

It can be easily derived also the dependence of responsivity with respect to the bandwidth of the device. It is shown in equation 5.7 and is plotted in Figure 5.2.

$$\mathcal{R}_{am} = \frac{1}{BW^2 \cdot \rho \cdot t} \frac{1}{\sqrt{\left(1 - \left(\frac{\omega}{\omega_0}\right)^2\right)^2 + \left(\frac{\omega}{Q \cdot \omega_0}\right)^2}} \quad (5.7)$$

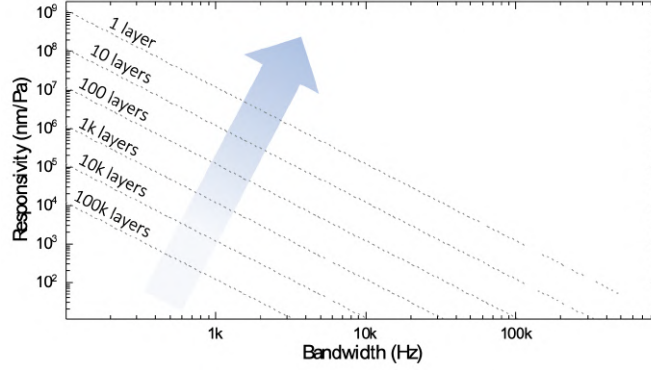


**Figure 5.2:** Microphone diaphragm responsivity vs Device bandwidth.

As can be seen, responsivity and bandwidth are inversely proportional, so, if it is needed a device with large bandwidth and high responsivity, a trade-off between the two has to be found. Alternatively, the number of membrane layers has to be minimized, so that both parameters are maximized at the same time.

It is possible to optimize the responsivity of the microphone also acting on the other two transduction stages.

Responsivity of the mechano-optical stage can be controlled by varying the gap between the optical fiber and the membrane. In fact, depending on this distance there is a greater or lesser coupled optical power, more precisely approaching the membrane it can be noticed a peak where the coupling factor ( $\eta$ ) is maximum. Taking into account the deflection of the membrane when subjected to pressure, the best solution is to place the optical fiber at a distance such as to have a coupled power slightly lower than peak value, so as to be at a point where the slope is large. This observation is made because responsivity is expressed exactly by that slope, as it indicates how much the coupled power varies due to a variation of the gap between the optical fiber and the membrane, when the latter vibrates being stimulated by an external pressure. As a result, the bigger is the slope and the higher is responsivity.

For what concerns responsivity of the opto-electrical stage, it can be optimized using high performance electronic components for light detection. Moreover,

to improve measurement accuracy and reduce the contribution of input power fluctuations on the modulated power, a setup with a reference part is exploited. In particular the reference consists in a second photodetector that measures the input optical power from the fiber and is used to detect fluctuations from the source, in order to subsequently normalize the output power modulated by the displacement of the membrane.

## 5.2 Fabrication and packaging

Before starting to assembly the microphone by installing the optical fiber, several layouts of the system are considered. The final version chosen is illustrated in Figure 5.3.

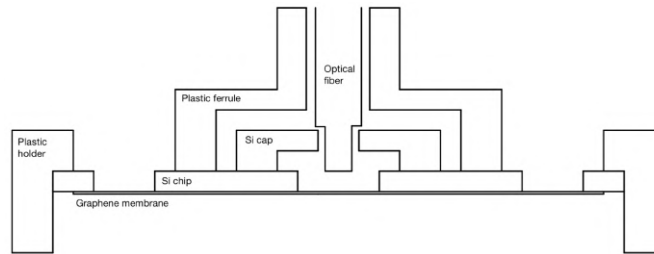


**Figure 5.3:** Microphone layout. The optical fiber is installed on the backside of the graphene membrane and is fixed and supported by a silicon cap and a plastic ferrule.

The fabrication of the microphone goes through several steps. It begins with the manufacture of graphene membranes, described in detail in paragraph 2.2. For the realization of the device it is selected a membrane made of bilayer graphene and with a diameter of  $750\mu m$ , one of the largest available to try to improve the responsivity of the device increasing the aspect ratio. Subsequently, to be able to better handle the silicon chip containing the membrane, a 3D plastic support is printed by EPFL additive manufacturing laboratory (AFA). This piece, indicated in Figure 5.3 as “Plastic holder”, consists of a square structure a few millimeters thick and with a hole in the middle of the same dimension of the silicon chip, so that the latter can be glued inside preventing its movement and avoiding, thanks to the thickness of the support, its contact with an external surface which could damage the graphene membrane. After gluing the silicon chip inside the plastic support, the next step is to install the optical fiber. Having to decide on which side to install it, the back of the chip is chosen, so as to leave intact the graphene membrane. Positioning the optical fiber perfectly aligned with the center of the hole where the membrane is located and perpendicular to it is not an easy process. To facilitate alignment, a silicon cap is used with a hole in the center with a diameter equal to the one of the optical fiber. This cap is glued to the back of the chip and

is used to prevent the optical fiber from moving after it has been aligned. In fact, it is passed through cap's hole arriving directly at the back of the membrane. In order to align the cap with the hole, micro actuators are used to move it slowly and with great precision. Meanwhile, with an optical microscope it is possible to look through the hole of the cap. The alignment occurs as soon as the graphene membrane can be seen through the hole. At this point the cap can be glued to the back of the chip, for this step a particular type of glue is used, in fact this hardens after a few seconds when struck by UV rays. This is fundamental because using a normal glue, it could flow through the other holes of the chip reaching the other side and coming into contact with the graphene membrane that could be damaged. So, using UV glue prevents it from flowing over the entire chip. To get a clearer idea an image of the cap glued to the back of the silicon chip is taken through the objective of the optical microscope and is shown in Figure 5.4.

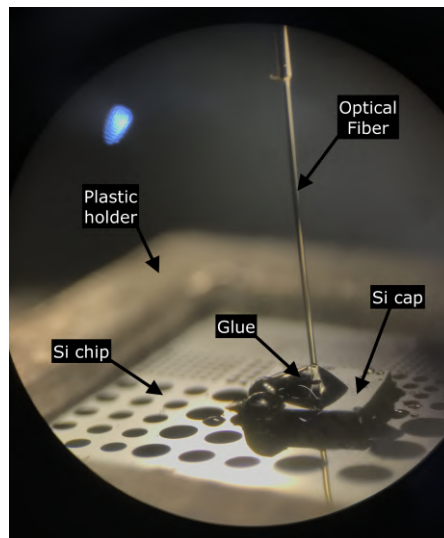


**Figure 5.4:** Optical fiber glued to silicon cap in correspondence of the graphene membrane on the backside of the silicon chip.

In Figure 5.4 it can be observed also the optical fiber which passes through the hole of the silicon cap and is glued onto it to fix its vertical position, paying attention to not pierce the membrane. Taking into account the observations made in paragraph 5.1.2 to improve the responsivity of the device, the coupled power is measured as a function of gap in order to find the optimal distance between optical fiber and membrane and get the greater responsivity. The optical fiber, being very delicate, is moved only by magnetic precision manipulators that do not bend and hold it firmly during gluing processes. To keep the optical fiber perpendicular to the surface avoiding bends that could worsen the signal, it is passed through a plastic ferrule, also printed by additive manufacturing, which keeps it rigid and

perpendicular at least when close to the membrane. At the end everything is glued to fix the various positions and avoid unwanted movements.

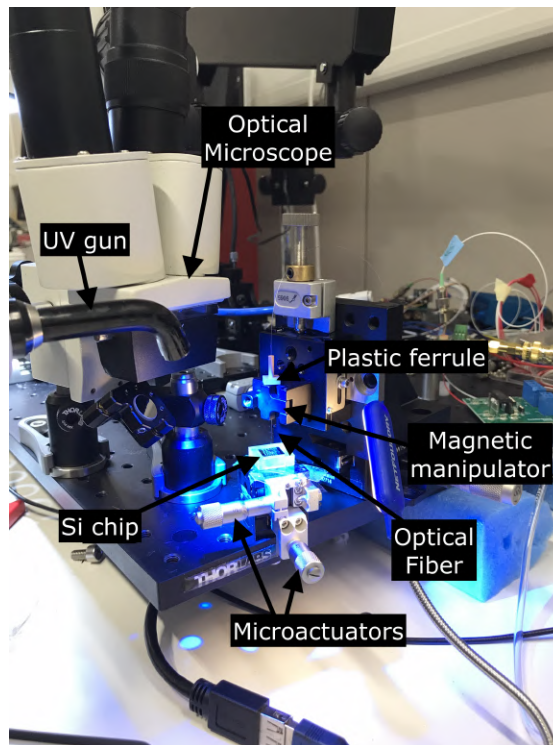


**Figure 5.5:** Setup for the installation of the optical fiber.

The image in Figure 5.5 shows the setup used for the installation of the optical fiber. It is possible to notice the microactuators used to move the chip and the magnetic manipulators used to hold the optical fiber. In particular it is shown the step before the installation of the plastic ferrule which at that moment was suspended on the chip, while the vertical position of the optical fiber is fixed by the glue that is hardened by the rays of the UV gun.

### 5.3 Characterization

The measures performed to characterize the microphone are only a starting point and should be deepened and improved.

To analyze the performances of the microphone it is necessary to convert the optical signal, modulated in intensity by membrane displacement, into an electrical signal. This task is performed by a component provided by Miraex, it is called *Gen2.1* and plays the role of the opto-electrical stage. This device consists of a metal box used to shield any external electromagnetic disturbance containing

two photodetectors and a Raspberry Pi. The two photodetectors are used for the conversion of the optical signal into electrical, they allow to have two acquisition channels and consequently to perform measurements with a reference configuration as suggested previously in paragraph 5.1.2. While, the Raspberry Pi is used to manage all the data coming from the microphone and to control any other components of the setup. It can be properly programmed through Python scripts to post-process all the data and analyze the results. Moreover, a useful feature is that it can be controlled remotely from an external device, if the latter is connected to the same network to which the board is connected via an Ethernet cable. Reduced size and portability are also interesting features of the box that make easier its use and transport.

### 5.3.1 Measure of graphene membrane reflectivity

Before mounting the setup for acquisition and analysis of the optical signal, the microphone is calibrated by studying the power reflected from the graphene membrane at steady-state conditions, without external stimuli. For this purpose a power meter from ThorLab, an optical circulator and a mirror are used. They are connected to each other as shown in Figure 5.6.

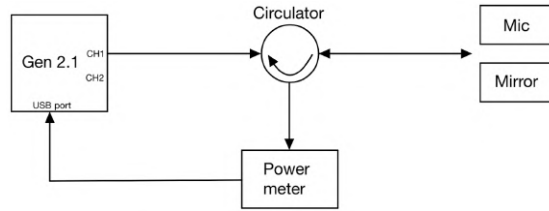


**Figure 5.6:** Setup for testing reflectivity of the graphene microphone.

Firstly, an optical signal with a certain power is sent by *Gen2.1* toward the mirror, the light beam is reflected and on the way back its path is deflected and directed to the power meter by the circulator. The beam intensity is computed and acquired by the Raspberry Pi. Afterwards, the same measure is performed substituting the mirror with the microphone. The power reflected by the mirror is equal to  $429.61\mu\text{W}$ , while for the microphone a power of  $12.23\mu\text{W}$  is measured. From these data, considering the mirror as perfect reflective, it is possible to conclude that reflectivity of the graphene membrane is around 2.85 %, a slightly low value, but consistent with the properties of graphene.

### 5.3.2 Frequency response analysis

After having ascertained that it is possible to receive a signal, even if low, from the graphene membrane, the study proceeds with the characterization of the device

from a frequency response point of view. The setup for these measurements uses a different configuration with different instruments. In addition to the *Gen2.1* box and the microphone to characterize, the other components introduced are: a speaker to generate sound waves, a reference microphone whose characteristics are known and an oscilloscope for reading signals from the graphene microphone and the reference one. The layout employed is shown in Figure 5.7.

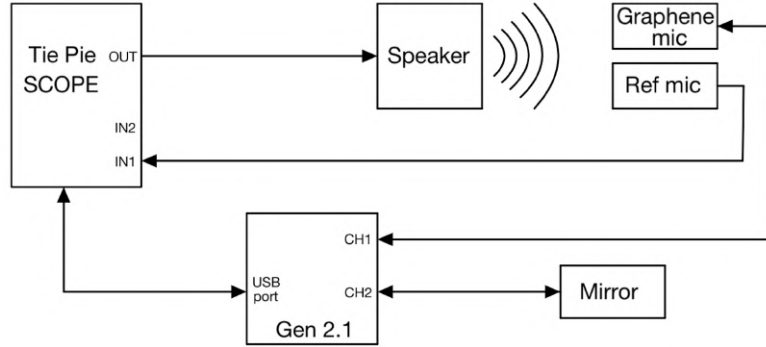


**Figure 5.7:** Setup to study the frequency response of the graphene microphone.

What is referred to as "TiePie SCOPE" is an USB oscilloscope from TiePie provided by Miraex, in particular it is the Handyscope HS3 model. This digital oscilloscope has two input and one output channels and is connected directly to the Raspberry Pi through a USB cable. It contains a signal acquisition system with a sampling rate up to 100 MSa/s and an arbitrary waveform generator, that can produce waves with a frequency of up to 2 MHz.

Nevertheless, in this project it is not possible to push up to such high frequencies because the available speaker is not able to reproduce them. The speaker utilized is provided by the EPFL signal processing laboratory (LTS2) and can reproduce sound waves up to a maximum of about 20 kHz.

Also the reference microphone from PCB Piezotronics is provided by the same laboratory. It is mainly used to compare its response to the one of graphene microphone, but also to test whether the measurement system is reliable or not, comparing the resulted measurements with those expected as the characteristics of the microphone are well known from the beginning.

Another element that is used in this setup is the mirror, this time it is exploited to implement a reference configuration taking advantage of the fact that the box *Gen2.1* has two channels. So, as can be seen in Figure 5.7, one channel is connected to the graphene microphone, while the other one to the mirror. In this way, noise from the optical fiber and the light source shall be detected and subtracted from the modulated signal.

To study the device's frequency response, measurements are taken in the anechoic

chamber of the signal processing laboratory. The setup is mounted inside as shown in the image reported in Figure 5.8.

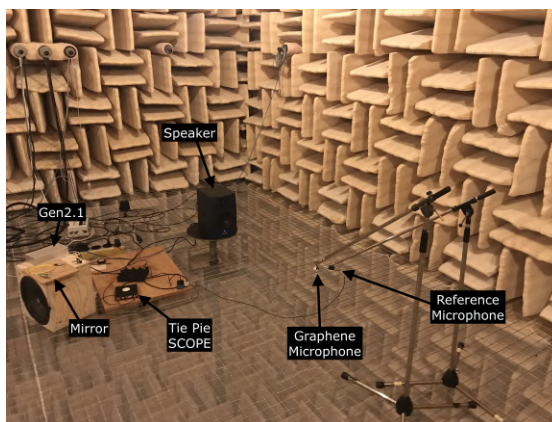


**Figure 5.8:** Setup mounted inside the anechoic chamber.

As it is possible to observe, the two microphones, the one in graphene and the reference one, are placed accurately side by side at the same distance from the source of the acoustic wave, in order to receive more or less the same contribution from the incident sound wave. The measurements are performed in an anechoic chamber to eliminate any other type of contribution that is not the signal to measure. The noise coming from the outside is shielded, while the reflection of the signal itself on the walls is completely absorbed by the particular coating that covers the entire room.

As soon as the setup is mounted inside the anechoic chamber, the next step involves the generation of the signal and the consequent study of the frequency response. To do this the Raspberry Pi is programmed through a Python script (Appendix A.3) to control the oscilloscope and generate the desired frequency sweep. At the same time it acquires also data from the two microphones that are subsequently processed and analysed. In this first study only the intensity of the signals is studied, but with further analysis it is possible to go into more detail, for example with a study on their phase. The reproduced frequency range varies from 25 Hz to 20 kHz with steps following the one-third octave bands to cover the entire range equally spaced. For each frequency the sound is recorded for 10 seconds by the two microphones. The acquired signals are processed through a matlab script, where a Fourier transform is applied.

The signal measured by the microphone is acquired for each frequency sent. In particular, there is a peak along the spectrum in correspondence of those frequencies. Since the measurements are affected by a consistent background noise, especially those of the graphene microphone, the plots of microphones frequency responses are not shown, because the relevant information concern only peak position and

height. So, for each signal the peak is identified at the corresponding frequency and the level of background noise is calculated. Data are reported in 5.1. For some frequencies the noise level is higher because the peak is not sharp, but smooth and its tails are partly considered in the calculation of the background noise, as to compute the latter, frequencies 5 Hz before and 5 Hz after the peak are taken into account and averaged.

Frequency (Hz)	Graphene response (V)	Graphene noise (V)	Reference response (V)	Reference noise (V)
25	1.81E-04	1.48E-04	3.28E-04	1.86E-05
31	2.20E-04	1.73E-04	3.62E-04	1.93E-05
40	3.08E-04	1.66E-04	8.04E-04	5.27E-05
50	1.59E-04	1.30E-04	1.27E-03	8.14E-05
63	1.88E-04	1.14E-04	2.69E-03	4.80E-04
80	8.13E-04	2.14E-04	5.50E-03	6.75E-04
100	1.64E-04	7.92E-05	5.87E-03	7.53E-04
125	1.52E-04	6.49E-05	8.04E-03	1.53E-04
160	1.66E-04	8.61E-05	6.80E-03	2.37E-04
200	2.71E-04	6.00E-05	6.09E-03	1.47E-04
250	2.31E-04	7.59E-05	5.79E-03	2.15E-04
315	1.32E-04	6.89E-05	6.12E-03	5.71E-05
400	8.68E-04	1.45E-04	5.42E-03	2.70E-04
500	4.48E-04	1.25E-04	5.39E-03	4.05E-04
630	1.13E-04	6.82E-05	5.75E-03	1.04E-04
800	1.51E-04	5.24E-05	6.75E-03	6.81E-04
1000	8.30E-04	1.33E-04	5.26E-03	8.36E-04
1250	8.92E-04	3.09E-04	5.99E-03	6.09E-04
1600	3.11E-04	7.94E-05	4.16E-03	9.13E-04
2000	3.46E-04	9.81E-05	5.70E-03	1.23E-03
2500	5.49E-04	9.74E-05	5.85E-03	7.93E-04
3150	1.76E-04	5.85E-05	5.44E-03	4.93E-04
4000	1.17E-04	5.83E-05	5.08E-03	6.49E-04
5000	6.58E-04	1.16E-04	3.13E-03	8.00E-04
6300	4.59E-03	5.04E-04	5.96E-03	1.16E-03
8000	2.18E-04	5.80E-05	6.87E-03	1.11E-03
10000	1.08E-04	4.12E-05	5.26E-03	1.09E-03
12500	6.42E-05	3.43E-05	3.96E-03	5.89E-04
16000	1.32E-04	3.82E-05	2.76E-03	5.88E-04
20000	5.11E-05	3.19E-05	1.61E-03	3.02E-04

**Table 5.1:** Graphene and reference microphone frequency response and ground noise.

As it is possible to observe the optical microphone peaks are much lower than those of the reference one and sometimes are submerged by background noise. While those of the reference microphone are easily distinguishable from the noise especially for the frequency range between 100 Hz and 20 kHz which are the frequencies for which it should work better.

## 5.4 Discussion

The proposed device needs some improvement, if on the one hand it is possible to conceptually get stunning results of responsivity, on the other it is not easy to make measurements due to the poor signal reflected by the graphene membrane

which is easily influenced by noise. The results obtained through the frequency sweep are not the best, there are some issues that affect measures and this leads to the impossibility of clearly distinguishing peaks for some frequencies.

First, it is checked if the problem comes from the setup, in particular from the speaker or the oscilloscope. To do that, the acquisition system is used to measure the response of the reference microphone under the stimulus of an acoustic wave generated by an acoustic calibrator. So, sending an accurate wave with a certain pressure and measuring the voltage response from the microphone using the USB oscilloscope, responsivity of the microphone is computed. The result is 39.6 mV/Pa, that is almost equal to 40 mV/Pa, the value reported in the datasheet. This first check demonstrates that the acquisition system is reliable.

Verification of the correct functioning of the setup proceeds with testing the speaker. To check this, pressures received by the reference microphone during the frequency sweep are extracted. Only the frequencies between 100 Hz and 20 kHz are considered since these are in the working range of the reference microphone. These pressures should be more or less the same with an uncertainty between  $\pm 3$  dB, as reported in the microphone datasheet. After making these considerations, the voltages measured through the reference microphone are divided by the responsivity of the device and all the pressures in Pascal are converted to dB. Finally, their standard deviation is calculated, it results to be 4.98 dB, that is a bit higher than the expected uncertainty range, but it is still good and, above all, can not be the cause of the problem with graphene microphone's peaks.

The problem can be attributed to the fact that the signals that are produced by the speaker are sine waves with a fixed frequency that is not gradually increased, but that is abruptly switched to the higher one. This can cause shot noise problems that cover microphone peaks. A solution to this problem would be a ramp that starts from the lowest frequency and gradually increases reaching the maximum frequency of the sweep.

But the main problem can be owed to the extremely low reflectivity of graphene. This leads to a reflected signal with very low intensity, that in turn generates a too small peak in frequency response spectrum, easily submerged by the noise that is present in every measure. A remedy to this issue could be the addition of a very thin layer of a material with a higher reflectivity in order to receive a higher and more easily measurable signal without affecting graphene properties. Or, instead of adding a layer, even a very tiny point mass would be helpful to reflect the light signal.

As mentioned above, this is only the beginning of research into an optical microphone based on a suspended graphene membrane. Once these problems are solved, it would be useful to continue with the improvement of the manufacturing and packaging process by finding a way to place the optical fiber in the best position more easily and in an automated way reducing to the minimum possible errors of

misalignment.

For what concerns the measurements to be performed to characterize the microphone, it would be interesting to study not only the intensity of the reflected signal but also its phase, to do so acquisition and sampling frequency of the two microphones have to be synchronized. These additional measures would form a more complete view of the device's performance.

However, the topic is very attracting and subject of continue research and development. This can lead to the realization of a microphone with formidable performance and with the possibility of being used for a large amount of applications ranging from the IoT world to the aerospace and military, which require a strong endurance by the device even to harsh environments, conditions that, in theory, this microphone can easily withstand.

# Chapter 6

## Conclusions

The main purpose of this thesis was to consolidate and deepen knowledge about properties of graphene, in particular, in the form of suspended membranes and, at the same time, propose possible implementations with them. Since the technological trend of recent years is moving towards the continuous miniaturization and diversification of devices, graphene has been proposed as an alternative material to those currently in use to go beyond their limits and open the door to new applications. The research carried out in this project has led to promising results both from the manufacturing point of view and from the point of view of possible applications, demonstrating how the structure of the proposed devices can combine simplicity and effectiveness. The structure of the thesis is mainly divided into three parts: the first one is about characterization of the surface of the membranes; the second part concerns the study of a phenomenon observed in those membranes and linked to the shift of their resonance frequency, which is used to detect vibrations or strains; the third and last part is dedicated to the development of a pressure sensor to be integrated with an optical fiber for the realization of an optical microphone graphene-based.

Initially the membranes were analyzed through an optical microscope and a DHM, the last one allowed to carry out an accurate study on the roughness of the membranes in a fast and interactive way, in fact, it is able to reproduce in real-time their surface with a nanometric accuracy. Through this analysis it was noticed how these devices can be stored over time by maintaining an acceptable surface condition and preserving their structural properties. Moreover, in this first part of membrane inspection, a method was also tested to improve membrane surface condition by subjecting it to a thermal annealing process that provided for a gradual increase of the temperature up to 350° C and a reduction of pressure down to  $5 \cdot 10^{-4}$  mbar, leaving the device inside a vacuum chamber with these conditions for 2 hours. The results obtained showed that in most cases membrane

roughness slightly decreases, but not significantly, suggesting a kind of saturation, which could be overcome by further increasing the temperature or by subjecting the membranes to longer thermal annealing cycles. Future research could move in this direction. This first part of membrane analysis is not only useful because it proposes effective methods for the characterization of graphene, but also to select the devices with better surface conditions to be used for the proposed applications.

The first proposal involves the use of membranes as vibrometers or strain sensors. It is demonstrated how it is possible to detect the presence of vibrations in a sample through the study of the resonance frequency of the membrane, in fact this is influenced and shifted when stimulated by an external movement. The device seems to be very sensitive with the possibility of detecting membrane displacements even in the order of nanometers. To achieve these results, a setup consisting mainly of a piezoshaker, which is used to provide external stimuli, and a LDV, to measure the membrane response, is exploited. In particular, the piezoshaker stimulates the membrane by vibrating at its resonance frequency and modulating the resonance with a second signal at a lower frequency, simulating an external vibration. The observed phenomenon is confirmed on different devices that differ in structure or material.

The same measurements are made on devices based on graphene with a mass attached to the membrane to facilitate its attenuation and the same results are obtained. The membranes of this project can be considered their evolution and demonstrate that mass is not necessary to detect the phenomenon under study, confirming themselves as valid alternatives even easier to manufacture and miniaturize.

Moreover, the same shift of the resonance frequency is also measured for membranes in silicon nitride, although with lower responsivity values. After some observations it was noted that this difference could be attributed to the built-in stress difference that characterizes each membrane. Therefore, this parameter is calculated for each membrane by deriving it from the resonance frequency formula and its influence on device's responsivity is studied. The results are aligned with the theoretically predicted curve showing an inversely proportional dependence of responsivity ( $\mathcal{R}_d$ ) with respect to built-in stress ( $\sigma_0$ ),  $\mathcal{R}_d \propto \sigma_0^{-1}$ .

For what concerns devices dimensions, having at disposal many membranes with different diameters, it is studied even if this parameter influences the responsivity, but from the measurements carried out it seems that the dimensions of the membranes do not have any influence, encouraging their possible further miniaturisation. The data collected in this part of the project seem to confirm the theory, but it needs further research, especially about the origin of the phenomenon observed. In fact, this study is part of a larger research that will be submitted to Nature Nanotechnology.

Finally, in the third part of the project, a totally optical microphone is assembled, which has as its main component the graphene membrane to which is installed an optical fiber on the back to detect its displacement. During the design of the layout and manufacturing, all the considerations previously made to optimize the performance of the device trying to maximize its responsivity are taken into account. In this direction one of the graphene membranes with the greatest aspect ratio is selected, having a diameter of 750  $\mu\text{m}$  and a thickness of about 0.67 nm (bilayer). In addition, the optical fiber is positioned at a distance that optimizes the coupled power that is reflected by the membrane. All this resulted in a small and robust device, despite the delicacy of the optical fiber that must be handled with care.

Afterwards, the obtained device is characterized by stimulating the membrane with sound waves at different frequencies generated by a loudspeaker and studying the intensity of the frequency response. The data obtained show peaks at the frequencies of the input signal with very low heights, that in some cases are covered by background noise. The main cause of this problem has been attributed to the fact that the graphene membrane has a very small reflection coefficient (2 %) and for this reason the signal carried by the optical fiber is very weak. For this reason, a later version of the device could foresee the deposition over the graphene membrane of a very thin layer of a material with a high coefficient of reflection that does not influence excessively the properties of the device, but at the same time stabilize the measurements and make them more accurate. Furthermore, since these measures are only a starting point for the characterisation of the device, a more in-depth study could be developed in the future to include not only the intensity of the signal reflected by the membrane, but also its phase, in such a way as to have a broader and more complete vision and to confirm what has been predicted by the theory.

# Appendix A

## Codes

In this appendix the main codes used during the project are reported.

### A.1 Sliding mean

The following Matlab script is used to calculate the roughness of the surface of the membranes by subtracting to the obtained profile its waviness. Measurements are repeated 5 times for each surface. The reported code is the one used to calculate the roughness during the steps of the thermal annealing process to observe its behavior.

```
1 clear all;
2 close all;
3
4 load('PhaseProf_complete.mat');
5
6 % Zoom on the high step (membrane surface)
7 PhaseProf_BeforeTA = PhaseProf_BeforeTA(24:523,2:6);
8 PhaseProf_200 = PhaseProf_200(33:532,2:6);
9 PhaseProf_300 = PhaseProf_300(36:535,2:6);
10 PhaseProf_350 = PhaseProf_350(43:542,2:6);
11 PhaseProf_350_30min = PhaseProf_350_30min(29:528,2:6);
12 PhaseProf_350_1h = PhaseProf_350_1h(28:527,2:6);
13 PhaseProf_350_1h_30min = PhaseProf_350_1h_30min(27:526,2:6);
14 PhaseProf_350_2h = PhaseProf_350_2h(27:526,2:6);
15
16 X = [PhaseProf_BeforeTA PhaseProf_200 PhaseProf_300 PhaseProf_350 ...
17      PhaseProf_350_30min PhaseProf_350_1h PhaseProf_350_1h_30min ...
18      PhaseProf_350_2h];
19
20 W = 50; % Window aperture
```

```

21 R = ones(1,5); % Roughness vector
22 R_mean = ones(1,8); % Roughness mean
23 R_stdev = ones(1,8); % Roughness standard deviation
24
25 x = linspace(0,300,500);
26
27 for n = 1:8 % Thermal annealing steps
28     for m = 1:5 % Number of measures on the same membrane
29
30         A = X(:,(n-1)*5+m);
31         L = length(A);
32         Sliding_mean_A = zeros(L,1);
33
34         for i = 1:L % Mean of the values inside the
range
35             sum = 0;
36             rep = 0;
37             for j = i-W/2:1:i+W/2-1
38                 if j >= 1 && j <= L
39                     sum = sum + A(j);
40                     rep = rep + 1;
41                 end
42             end
43             Sliding_mean_A(i) = sum/rep; % Waviness of the surface
44         end
45
46         R(m) = std(A-Sliding_mean_A); % Waviness removal
47
48         figure(n)
49         plot(x,A,'-r'); hold on; % Waviness + roughness
50         plot(x,Sliding_mean_A,'.k'); hold on; % Waviness
51         plot(x,A-Sliding_mean_A,'-b'); % Roughness
52         xlabel('x (um)');
53         ylabel('z (nm)');
54         legend('Surface profile','Waviness','Roughness');
55     end
56     R_mean(n) = mean(R);
57     R_stdev(n) = std(R);
58
59 end
60
61 step = linspace(1,8,8);
62 figure
63 plot(step,R_mean,'o'); % Plot roughness behavior during thermal
annealing
64 errorbar(R_mean,R_stdev);
65 xlabel('Thermal annealing steps');
66 ylabel('Roughness (nm)');

```

## A.2 Acceleration due to a change in voltage

The Matlab script reported below communicate with the lock-in amplifier software interface setting the required parameters. It is also used to measure the shift of membrane resonance frequency due to a change in voltage of the second signal provided to the piezoshaker. All the data is collected and saved in files ready to be analyzed and evaluated.

```

1 clear all; close all;
2 device_id = 'dev2063';
3
4 % Setting parameters
5 VdriveResonance = 1;           % Voltage first signal
6 FreqAcceleration = 160;       % Frequency second signal
7
8 SamplingRate = 13e3;
9 %LowPassFilter = 10e3;
10
11 sweepPoints = 300;
12 StartFreq = 150e3;
13 EndFreq = 200e3;
14
15 SecondsPlotter = 10;
16
17 voltages = linspace(0.1,0.5, 9); % Voltage sweep second signal
18
19 % Saving data
20 path = 'D:\Vincenzo \...';
21
22 filenameM = 'MatlabResult1.txt';
23 fileIDM = fopen([path filenameM], 'w');
24 fprintf(fileIDM, '—Frequency: %f\n', FreqAcceleration);
25
26 Freq_shifts = [];
27 Freq_reson = [];
28 NoiseBIN = [];
29
30 index = 0;
31
32 % Setting lock-in amplifier parameters communicating with the LabOne
   software
33 for VdriveAccel = voltages
34 index = index+1;
35 LowPassFilter = 5*FreqAcceleration;
36
37 data = Sweeper(device_id, StartFreq, EndFreq, FreqAcceleration, '
   amplitude', VdriveResonance, 'sweep_samplecount', sweepPoints);

```

```

38 Sweep_freq = data.dev2063.demods.sample{1, 1}.frequency;
39 Sweep_ampl = data.dev2063.demods.sample{1, 1}.r;
40 Sweep_phase = data.dev2063.demods.sample{1, 1}.phase*60;
41
42 [val, idx] = max(Sweep_ampl);
43 resonantFreq = Sweep_freq(idx);      % Frequency first signal (
44     resonance)
45
46 ziDAQ('setDouble', '/dev2063/oscs/0/freq', resonantFreq);
47
48 ziDAQ('setInt', '/dev2063/demods/1/oscselect', 1);
49 ziDAQ('setDouble', '/dev2063/oscs/1/freq', FreqAcceleration);
50 ziDAQ('setInt', '/dev2063/demods/0/order', 1);
51 ziDAQ('setDouble', '/dev2063/demods/0/timeconstant', 0.159154943/
52     LowPassFilter);
53 ziDAQ('setInt', '/dev2063/demods/1/order', 1);
54 ziDAQ('setDouble', '/dev2063/demods/1/timeconstant', 0.159154943/
55     LowPassFilter);
56 ziDAQ('setInt', '/dev2063/demods/0/enable', 1);
57 ziDAQ('setDouble', '/dev2063/demods/0/rate', SamplingRate);
58 ziDAQ('setInt', '/dev2063/demods/1/enable', 1);
59 ziDAQ('setDouble', '/dev2063/demods/1/rate', SamplingRate);
60
61 ziDAQ('setDouble', '/dev2063/sigouts/0/amplitudes/0', VdriveResonance
62     );
63 ziDAQ('setDouble', '/dev2063/sigouts/0/amplitudes/1', VdriveAccel);
64 ziDAQ('setInt', '/dev2063/sigouts/0/enables/1', 1);
65 ziDAQ('setInt', '/dev2063/sigouts/0/on', 1);
66
67 [Data] = getZIPlotterData(SecondsPlotter);
68
69 PlotterPhase = Data(:,4); % -180;
70 TimePhase = Data(:,1);
71
72 % Deriving the shift of the resonance frequency from the recorded
73     phase
74 OscFreq = interp1(Sweep_phase, Sweep_freq, PlotterPhase);
75 i=1;
76 while mean(isnan(OscFreq))>0.2 % Subtract a multiple of 180 when
77     phase=NaN
78     OscFreq = interp1(Sweep_phase, Sweep_freq, PlotterPhase-i*180);
79     i=i+1;
80 end
81
82 filename = ['OscFreq' num2str(FreqAcceleration) 'Voltage' num2str(
83     VdriveAccel*1000) '.txt'];
84 fileID = fopen([path filename], 'w');
85 fprintf(fileID, '%d ; %d\n', [TimePhase ; OscFreq]);

```

```

80 fclose(fileID);
81
82 F = OscFreq;           % Modulation of the resonance frequency over
    time
83
84 X = TimePhase;
85
86 dimension = length(OscFreq);
87
88 Fs = dimension/X(end); % Sampling frequency
89 Ts = 1/Fs;           % Sampling period
90 Fn = Fs/2;          % Nyquist Frequency
91
92 F(isnan(F)) = [];    % Eliminate NaN Values First
93
94 FF = fft(F)/dimension; % Fourier Series of Data, Freq Vector
95 Fv = linspace(0,1,fix(dimension/2)+1)*Fn;
96 Iv = 1:length(Fv);  % Index Vector
97
98 % Plot FFT
99 h = figure();
100 loglog(Fv, abs(FF(Iv)))
101 grid
102 xlabel('Frequency (Hz)')
103 ylabel('Amplitude (Hz)')
104 title("Modulation Frequency of " + num2str(FreqAcceleration) + " Hz"
    + ' Voltage of ' + num2str(VdriveAccel*1000))
105 xlim([FreqAcceleration-100 FreqAcceleration+1000])
106
107 filename = ['Freq_' num2str(FreqAcceleration) '_Voltage_' num2str(
    VdriveAccel*1000) '.fig'];
108 savefig([path filename])
109
110 FFTarray = abs(FF(Iv));
111
112 % Shift of resonance frequency
113 FFT_peak = max(FFTarray(Fv>FreqAcceleration-0.2 & Fv<FreqAcceleration
    +0.2));
114
115 Noise = mean(FFTarray(Fv>FreqAcceleration-100 & Fv<FreqAcceleration
    +1000));
116
117 fprintf('—Progress %0.0f%%\n', index/length(voltages)* 100);
118 fprintf('—Frequency: %f\n', FreqAcceleration);
119 fprintf('—Voltage: %f\n', VdriveAccel);
120 fprintf('—Freq Shift: %f\n', FFT_peak);
121 fprintf('—Rel Freq Shift: %f\n', FFT_peak/resonantFreq);
122 fprintf('—Noise: %f\n', Noise);
123 fprintf('—SNR: %f\n', FFT_peak/Noise);

```

```

124 |
125 | Freq_shifts = [Freq_shifts FFT_peak];
126 | Freq_reson = [Freq_reson resonantFreq];
127 | NoiseBIN = [NoiseBIN Noise];
128 |
129 | fprintf(fileIDM, '—Resonant Freq: %f\n —Voltage: %f\n —Freq Shift:
      | %f\n —Rel Freq Shift: %f\n —Noise: %f\n —SNR: %f\n\n', [
      | resonantFreq; VdriveAccel; FFT_peak; FFT_peak/resonantFreq; Noise;
      | FFT_peak/Noise]);
130 | end
131 |
132 | % Saving data
133 | save FreqShifts.mat Freq_shifts;
134 | save ResonantFreq.mat Freq_reson;
135 | save Noise.mat NoiseBIN;
136 |
137 | fclose(fileIDM);

```

### A.3 Microphone frequency response

This Python script is used to control the TiePie SCOPE, in particular, the waveform generator to let the speaker produce the desired acoustic wave and the acquisition system to read the signal detected by the reference microphone. At the same time, the signals coming from the optical microphone and the one reflected by the mirror are also acquired by the photodetectors in the two channels of the Gen2.1.

```

1 | #!/usr/bin/env python3
2 |
3 | import numpy as np
4 | from miraex_pydriver import driver, Signal
5 | from miraex_instrument_drivers import ScopeGen
6 | from concurrent.futures import ThreadPoolExecutor
7 | from time import sleep
8 | from pathlib import Path
9 | from tqdm import tqdm
10 |
11 |
12 | SLED_POWER_TARGET = 1.0
13 | SLED_SETTLE_TIME = 60
14 | SAMPLING_TIME = 10
15 | OUTPUT_DIR = Path('sweep-data')
16 | SINE_AMPLITUDE = 10e-3
17 | FREQUENCIES = np.logspace(2, 4.4, 200)
18 | VRANGE = 0.1
19 |

```

```
20
21 def measure(drv, scopegen, freq, time):
22
23     # set frequency
24     print(f'Setting frequency to {freq:.0f}Hz ...')
25     scopegen.gen.frequency = freq
26     scopegen.gen.start()
27     sleep(0.1)
28
29     # flush data
30     print('Flushing...')
31     for _ in tqdm(range(100)):
32         drv.get_ac()
33
34     with ThreadPoolExecutor() as executor:
35
36         # start acquisition
37         ac_future = executor.submit(measure_ac, drv, SAMPLING_TIME)
38         ref_future = executor.submit(measure_ref, scopegen,
39 SAMPLING_TIME)
40
41         # wait for results
42         ac1, ac2 = ac_future.result()
43         ref = ref_future.result()
44
45     # record data
46     print(f'Recording {SAMPLING_TIME:.2f}s of data ...')
47     return ref, ac1, ac2
48
49
50 def measure_ref(scope, time):
51
52     scope.Vrange = VRANGE
53     scope.measurement_time = SAMPLING_TIME
54     scope.presample_ratio = 0
55
56     values = scope.get_data()[0]
57     times = np.arange(len(values)) / scope.sampling_rate
58
59     return [times, values]
60
61
62 def measure_ac(drv, time):
63
64     n = SAMPLING_TIME / drv.get_ac_sampling_period()
65
66     ac1, ac2 = drv.get_ac()
67
```

```
68 ac1_chunks = [ac1]
69 ac2_chunks = [ac2]
70
71 def compute_length():
72     return sum(len(a) for a in ac1_chunks)
73
74 while compute_length() < n:
75
76     signals = drv.get_signals(10000)
77     ac1_chunks.append(signals.ac1)
78     ac2_chunks.append(signals.ac2)
79
80     print('Merging data chunk ...', flush=True)
81
82     ac1 = Signal()
83     ac2 = Signal()
84
85     for chunk1, chunk2 in zip(ac1_chunks, ac2_chunks):
86         ac1 += chunk1
87         ac2 += chunk2
88
89     return ac1, ac2
90
91
92 def signal_to_array(signal):
93     return np.array([signal.times - signal.times[0], signal.values])
94
95
96 def main():
97
98     # empty data dir
99     print(f'Emptying data dir: {OUTPUT_DIR} ...')
100    for f in OUTPUT_DIR.iterdir():
101        f.unlink()
102
103    # open and setup TiePie
104    scopegen = ScopeGen(n_channels=1, sampling_rate=64e3)
105
106    scopegen.generator_mode = 'sine'
107    scopegen.gen.amplitude = SINE_AMPLITUDE
108
109    with driver() as drv:
110
111        # set SLED power
112        print(f'Setting SLED output target to {SLED_POWER_TARGET
113        :.2%}...')
114        drv.set_sled_target(1.0)
115        sleep(SLED_SETTLE_TIME)
```

```
116     for n, freq in enumerate(FREQUENCIES):
117
118         # measure
119         ref, ac1, ac2 = measure(drv, scopegen, freq,
SAMPLING_TIME)
120
121         # save data
122         filename = OUTPUT_DIR / f'{n:03d}.npz'
123         print(f'Saving to {filename.absolute()} ...')
124         data = {
125             'freq': freq,
126             'ref': ref,
127             'ac1': signal_to_array(ac1),
128             'ac2': signal_to_array(ac2),
129         }
130         np.save(str(filename), data)
131
132
133 if __name__ == '__main__':
134     main()
```

# Bibliography

- [1] Serena Brischetto. *The Future of MEMS*. 2019. URL: <https://www.semi.org/en/blogs/technology-trends/the-future-of-mems>. accessed: 27.08.2021 (cit. on pp. 1, 2).
- [2] Shilpa Nagod and SV Halse. «Evolution of MEMS Technology». In: *Evolution* 4.12 (2017) (cit. on p. 2).
- [3] *History of MEMS*. URL: [https://nanohub.org/resources/26535/download/App\\_Intro\\_PK10\\_PG.pdf](https://nanohub.org/resources/26535/download/App_Intro_PK10_PG.pdf). accessed: 26.08.2021 (cit. on p. 2).
- [4] W Fang, S-S Li, C-L Cheng, C-I Chang, W-C Chen, Y-C Liu, M-H Tsai, and C Sun. «CMOS MEMS: A key technology towards the “More than Moore” era». In: *2013 Transducers & Eurosensors XXVII: The 17th International Conference on Solid-State Sensors, Actuators and Microsystems (TRANSDUCERS & EUROSENSORS XXVII)*. IEEE. 2013, pp. 2513–2518 (cit. on p. 2).
- [5] Xuge Fan. «Integration of graphene into MEMS and NEMS for sensing applications». PhD thesis. KTH Royal Institute of Technology, 2018 (cit. on pp. 2, 4).
- [6] GJ Shu, SC Liou, S Karna, R Sankar, M Hayashi, M-W Chu, and FC Chou. «Graphene-like conjugated  $\pi$  bond system in  $\text{Pb}_{1-x}\text{Sn}_x\text{Se}$ ». In: *Applied Physics Letters* 106.12 (2015), p. 122101 (cit. on p. 3).
- [7] Changgu Lee, W Xiaoding, and W Jeffrey. «Measurement of the Elastic Properties and Intrinsic Strength of Monolayer Graphene». In: *Science* 321 (2008), pp. 385–388 (cit. on p. 3).
- [8] Alexander A. Balandin, Suchismita Ghosh, Wenzhong Bao, Irene Calizo, Desalegne Teweldebrhan, Feng Miao, and Chun Ning Lau. «Superior Thermal Conductivity of Single-Layer Graphene». In: *Nano Letters* 8.3 (2008). PMID: 18284217, pp. 902–907. DOI: 10.1021/nl0731872. URL: <https://doi.org/10.1021/nl0731872> (cit. on p. 4).

- 
- [9] Chengzhu Liao, Yuchao Li, and Sie Chin Tjong. «Graphene Nanomaterials: Synthesis, Biocompatibility, and Cytotoxicity». In: *International Journal of Molecular Sciences* 19.11 (2018). ISSN: 1422-0067. DOI: 10.3390/ijms19113564. URL: <https://www.mdpi.com/1422-0067/19/11/3564> (cit. on p. 4).
- [10] Satender Kataria et al. «Chemical vapor deposited graphene: From synthesis to applications». In: *physica status solidi (a)* 211.11 (2014), pp. 2439–2449 (cit. on p. 4).
- [11] Kostya S Novoselov, Andre K Geim, Sergei V Morozov, De-eng Jiang, Yan-shui Zhang, Sergey V Dubonos, Irina V Grigorieva, and Alexandr A Firsov. «Electric field effect in atomically thin carbon films». In: *Science* 306.5696 (2004), pp. 666–669 (cit. on p. 5).
- [12] Kazuma Matsui, Yusuke Takei, Akira Inaba, Tomoyuki Takahata, Kiyoshi Matsumoto, and Isao Shimoyama. «Processing of graphene into a cantilever beam structure using a focused ion beam». In: *Micro & Nano Letters* 11.11 (2016), pp. 670–674 (cit. on p. 5).
- [13] Verbridge SS et al Bunch JS van der Zande AM. «Electromechanical resonators from graphene sheets». In: *Science* 315.5811 (2007), pp. 490–493 (cit. on p. 5).
- [14] Quan Wang and Behrouz Arash. «A review on applications of carbon nanotubes and graphenes as nano-resonator sensors». In: *Computational Materials Science* 82 (2014), pp. 350–360 (cit. on p. 5).
- [15] Wen-Ming Zhang, Kai-Ming Hu, Zhi-Ke Peng, and Guang Meng. «Tunable micro-and nanomechanical resonators». In: *Sensors* 15.10 (2015), pp. 26478–26566 (cit. on p. 5).
- [16] Daniel Moreno, Xuge Fan, Frank Niklaus, and Luis Guillermo Villanueva. «Proof of Concept of a Graphene-Based Resonant Accelerometer». In: *2021 IEEE 34th International Conference on Micro Electro Mechanical Systems (MEMS)*. IEEE. 2021, pp. 838–840 (cit. on pp. 5, 26, 33).
- [17] Xuge Fan et al. «Manufacture and characterization of graphene membranes with suspended silicon proof masses for MEMS and NEMS applications». In: *Microsystems & Nanoengineering* 6.1 (2020), pp. 1–17 (cit. on p. 5).
- [18] Qin Zhou, Jinglin Zheng, Seita Onishi, MF Crommie, and Alex K Zettl. «Graphene electrostatic microphone and ultrasonic radio». In: *Proceedings of the National Academy of Sciences* 112.29 (2015), pp. 8942–8946 (cit. on p. 6).
- [19] Cheng Li, Jun Xiao, Tingting Guo, Shangchun Fan, and Wei Jin. «Interference characteristics in a Fabry–Perot cavity with graphene membrane for optical fiber pressure sensors». In: *Microsystem technologies* 21.11 (2015), pp. 2297–2306 (cit. on p. 6).

- 
- [20] Debo Wang, Xingyue He, Jiang Zhao, Leisheng Jin, and Xincun Ji. «Research on the Electrical-Thermal-Acoustic Conversion Behavior of Thermoacoustic Speakers Based on Multilayer Graphene Film». In: *IEEE Sensors Journal* 20.24 (2020), pp. 14646–14654 (cit. on p. 6).
- [21] Christian Berger, Rory Phillips, Alba Centeno, Amaia Zurutuza, and Aravind Vijayaraghavan. «Capacitive pressure sensing with suspended graphene-polymer heterostructure membranes». In: *Nanoscale* 9.44 (2017), pp. 17439–17449 (cit. on p. 6).
- [22] Stephane Neuville. «Selective carbon material engineering for improved MEMS and NEMS». In: *Micromachines* 10.8 (2019), p. 539 (cit. on pp. 6, 7).
- [23] Li Lin et al. «Towards super-clean graphene». In: *Nature communications* 10.1 (2019), pp. 1–7 (cit. on p. 6).
- [24] Phuong Viet Pham. «Cleaning of graphene surfaces by low-pressure air plasma». In: *Royal Society open science* 5.5 (2018), p. 172395 (cit. on p. 6).
- [25] W Xie et al. «Clean graphene surface through high annealing temperature». In: *Carbon* 94 (2015), pp. 740–748 (cit. on pp. 6, 22).
- [26] Shirin Afyouni Akbari, Vahid Ghafarinia, Tom Larsen, Marsha M Parmar, and Luis Guillermo Villanueva. «Large Suspended Monolayer and Bilayer Graphene Membranes with Diameter up to 750  $\mu\text{m}$ .» In: *Scientific Reports* 10.1 (2020) (cit. on pp. 7, 9, 14, 25).
- [27] Yanxia Wu, Shengxi Wang, and Kyriakos Komvopoulos. «A review of graphene synthesis by indirect and direct deposition methods». In: *Journal of Materials Research* 35.1 (2020), pp. 76–89 (cit. on p. 10).
- [28] Tabinda Sattar. «Current review on synthesis, composites and multifunctional properties of graphene». In: *Topics in Current Chemistry* 377.2 (2019), pp. 1–45 (cit. on p. 10).
- [29] Nikon Corporation. *ECLIPSE LV-N, Industrial Microscope*. 2019. URL: <https://www.nikonmetrology.com/images/brochures/lv-n-en.pdf>. accessed 20.07.2021 (cit. on p. 13).
- [30] Jun Ma, Wei Jin, Hoi Lut Ho, and Ji Yan Dai. «High-sensitivity fiber-tip pressure sensor with graphene diaphragm». In: *Optics letters* 37.13 (2012), pp. 2493–2495 (cit. on p. 13).
- [31] LyncéeTec. *Reflection DHM[r]*. 2013. URL: <https://www.lynceetec.com/reflection-dhm/>. accessed 30.08.2021 (cit. on p. 15).
- [32] Etienne Cuche, Pierre Marquet, and Christian Depeursinge. «Simultaneous amplitude-contrast and quantitative phase-contrast microscopy by numerical reconstruction of Fresnel off-axis holograms». In: *Applied optics* 38.34 (1999), pp. 6994–7001 (cit. on p. 16).

- [33] P Sahoo. «Surface topography». In: *Tribology for Engineers*. Elsevier, 2011, pp. 1–32 (cit. on pp. 18–20).
- [34] Prof. P. Mandracci. *Morphological surface analysis at the nanoscale*. Course of Materials and characterizations for Micro and Nanotechnologies, Politecnico di Torino. 2019 (cit. on pp. 18, 20).
- [35] Novacam. *Measuring circumferential roughness on inside diameters of hard-to-reach spaces*. 2020. URL: <https://www.novacam.com/2020/07/05/measuring-surface-roughness-on-id-circumference>. accessed: 15.07.2021 (cit. on p. 18).
- [36] Daniel Moreno Garcia. *Modelling, Simulations and Characterization of NEMS accelerometers based on graphene*. Tech. rep. 2020 (cit. on p. 27).
- [37] Antonia Lima-Rodriguez, Antonio Gonzalez-Herrera, and Jose Garcia-Manrique. «Study of the dynamic behaviour of circular membranes with low tension». In: *Applied Sciences* 9.21 (2019), p. 4716 (cit. on p. 29).
- [38] Silvan Schmid, Luis Guillermo Villanueva, and Michael Lee Roukes. *Fundamentals of nanomechanical resonators*. Vol. 49. Springer, 2016 (cit. on pp. 30, 31, 59).
- [39] *Laser Doppler vibrometry - Technology from Polytec - Polytec*. URL: <https://www.polytec.com/eu/vibrometry/technology/laser-doppler-vibrometry>. accessed: 27.07.2021 (cit. on p. 34).
- [40] Ottoleo Kuter-Arnebeck, Aleksander Labuda, Surabhi Joshi, Kaushik Das, and Srikar Vengallatore. «Estimating Damping in Microresonators by Measuring Thermomechanical Noise Using Laser Doppler Vibrometry». In: *Journal of Microelectromechanical Systems* 23.3 (2014), pp. 592–599. DOI: 10.1109/JMEMS.2013.2286199 (cit. on p. 36).
- [41] T. I. Team. *Standard Error of the Mean vs. Standard Deviation: The Difference*. URL: <https://www.investopedia.com/ask/answers/042415/what-difference-between-standard-error-means-and-standard-deviation.asp>. accessed: 03.08.2021 (cit. on p. 45).
- [42] M Olfatnia, Z Shen, JM Miao, LS Ong, T Xu, and M Ebrahimi. «Medium damping influences on the resonant frequency and quality factor of piezoelectric circular microdiaphragm sensors». In: *Journal of micromechanics and microengineering* 21.4 (2011), p. 045002 (cit. on p. 50).
- [43] Airat Shafikov, Bart Schurink, Robbert WE van de Kruijs, J Benschop, WTE van den Beld, Zomer Silvester Houweling, and F Bijkerk. «Strengthening ultrathin Si<sub>3</sub>N<sub>4</sub> membranes by compressive surface stress». In: *Sensors and Actuators A: Physical* 317 (2021), p. 112456 (cit. on p. 51).

- [44] Walter Hunt, Karthik Kadirval, Stephen Horowitz, Robert Taylor, Toshikazu Nishida, and Mark Sheplak. «Design and characterization of MEMS optical microphone for aeroacoustic measurement». In: *42nd AIAA Aerospace Sciences Meeting and Exhibit*. 2004, p. 1030 (cit. on p. 58).